Early Cretaceous subduction of Paleo-Pacific Ocean in the coastal region of SE China: Petrological and geochemical constraints from the mafic intrusions

Article *in* Lithos · March 2019

DOI: 10.1016/j.lithos.2019.03.010

CITATIONS
10

READS
390

6 authors, including:

Feng Guo
Chinese Academy of Sciences
118 PUBLICATIONS **4,470** CITATIONS
SEE PROFILE

Xiaobing Zhang
Chinese Academy of Sciences
5 PUBLICATIONS **11** CITATIONS
SEE PROFILE

Yangming Wu
Sun Yat-Sen University
7 PUBLICATIONS **31** CITATIONS
SEE PROFILE

Liang Zhao
Guangzhou Instutite of Geochemistry, Chinese Acadamy of Sciences
33 PUBLICATIONS **660** CITATIONS
SEE PROFILE

Lithos 334–335 (2019) 8–24

Contents lists available at ScienceDirect

Lithos

journal homepage: www.elsevier.com/locate/lithos

Early Cretaceous subduction of Paleo-Pacific Ocean in the coastal region of SE China: Petrological and geochemical constraints from the mafic intrusions

Bo Zhang [a,b], Feng Guo [a,*], Xiaobing Zhang [a,b], Yangming Wu [a,b], Guoqing Wang [a,b], Liang Zhao [a]

[a] State Key Laboratory of Isotope Geochemistry, Guangzhou Institute of Geochemistry, Chinese Academy of Sciences, Guangzhou 510640, PR China
[b] Graduate University of Chinese Academy of Sciences, Beijing 100049, PR China

ARTICLE INFO

Article history:
Received 20 December 2018
Accepted 9 March 2019
Available online 12 March 2019

Keywords:
Subducted sediment
Paleo-Pacific Ocean
Petrology and geochemistry
Gabbro
Early cretaceous
SE China

ABSTRACT

The Mesozoic tectono-magmatism in SE China has widely been considered to relate to subduction of the Paleo-Pacific Ocean. However, there lacks robust petrologic and geochemical evidence from subduction-related mafic igneous rocks to reconstruct the architecture of the subduction zone. This paper presents a comprehensive geochemical dataset (petrography, mineral chemistry, zircon U-Pb age, in-situ Sr and Pb isotope compositions of plagioclase and whole-rock major, trace element and Sr-Nd-Pb-Hf isotope data) of three early Cretaceous (Pingtan, Daiqianshan and Quanzhou) mafic intrusions from the coastal region in SE China, with aims to understand their petrogenetic link with subduction of the Paleo-Pacific Ocean. The mafic rocks comprise predominantly calcic hornblende and Ca-rich plagioclase and show varying degrees of crystal accumulation. Petrological observations and mass balance calculation indicate their parental magmas are hydrous and calc-alkaline with typical arc-type trace element features. These rocks are also characterized by "crust-like" isotopic signatures, i.e., moderately radiogenic Sr, unradiogenic Nd and highly radiogenic Pb compositions. The narrow variations of in-situ plagioclase Sr and Pb isotope ratios and the nearly identical isotope compositions between the plagioclase and bulk rock in each intrusion indicate a minor role of crustal assimilation during magmatic evolution. Instead, such "crust-like" isotopic signatures were largely resulted from source enrichment through an input of subducted sediment. Further element-isotopic modeling results suggest that the parental magmas were likely produced by melting of a depleted mantle source metasomatized via the subducted sediment-derived melt. Generation of the early Cretaceous mafic intrusions can thus be explained by subduction of a relatively hot oceanic slab, during which melt derived from the subducted sediment acted as a predominant agent to enrich the mantle wedge. Our results provide powerful petrological and geochemical constraints on the early Cretaceous subduction of the Paleo-Pacific Ocean beneath the SE China and suggest that addition of subducted sediment-derived melt may be an important mechanism for mantle enrichment in relatively hot subduction zones.

1. Introduction

Crustal recycling is an indispensable process to chemical evolution of the Earth, with the subduction zone as a key conduit. The geochemical imprints of subducted sediment have widely been identified in subduction-related igneous rocks (e.g., Shimoda et al., 1998; White and Dupré, 1986). Mass balance calculation suggests that ~ 20% of the subducted sediment has been involved in the arc magmas during the Earth's evolution (Nichols et al., 1994). Recycling of the subducted sediment therefore plays an important role in subarc mantle enrichment and geochemical evolution of lithospheric mantle (e.g., Davidson, 1987; Plank and Langmuir, 1998).

The mechanisms for subarc mantle enrichment through addition of the subducted sediment include aqueous fluid- (e.g., Barry et al., 2006; Grove et al., 2002) and melt-mediated types (e.g., Hermann and Spandler, 2008; Mallik et al., 2016; Shimoda et al., 1998) and/or both (e.g., Guo et al., 2016; Labanieh et al., 2010; Mazzeo et al., 2014). The enrichment style depends largely upon the thermal structure of a subduction zone (Plank et al., 2009; Watt et al., 2013), i.e., fluid-mediated enrichment is predominant in relatively cold subduction zones such as in Izu-Bonin-Mariana, Tonga, Central and Northern Scotia (e.g., Barry et al., 2006; Clift et al., 2001; Hauff et al., 2003; Tamura et al., 2007); whereas melting of the subducted sediment is more prevalent in relatively hot subduction zones like the SW Japan, Lesser Antilles, and Banda arcs (e.g., Labanieh et al., 2010; Nebel et al., 2011; Shimoda et al., 1998; Vroon et al., 1993). Accordingly, many mafic magmas formed in relatively hot subduction zones generally display

* Corresponding author.
E-mail address: guofengt@263.net (F. Guo).

https://doi.org/10.1016/j.lithos.2019.03.010
0024-4937/

"crust-like" isotopic signatures (e.g., Bezard et al., 2015; Shimoda et al., 1998; Vroon et al., 1993); whereas those from the cold subduction zones usually show "depleted mantle-like" isotopic features (e.g., Barry et al., 2006; Hauff et al., 2003; Ribeiro et al., 2013). Nevertheless, it is not always straightforward to distinguish the mechanism of mantle enrichment through the geochemistry of subduction-related magmas. One of the reasons is the complexity of mantle metasomatism (Labanieh et al., 2010; Walowski et al., 2015), e.g., the slab fluid can be released from both the sediment and altered oceanic lithosphere, and the slab melt may also originate from both the subducted oceanic crust and its overlying sediment. Another is the open-system magmatic evolution (e.g., Chiaradia et al., 2011; Humphreys et al., 2006), such as crustal contamination and assimilation-fractional crystallization (AFC). All these factors contribute to the ambiguous interpretation of the geochemical features in subduction-related mafic magmas. It is thus essential to distinguish the role of "source contamination" from "crustal assimilation" in such mafic magmas before we can further investigate the thermal structure, crust-mantle interaction and crustal recycling beneath the subduction zones.

The coastal region of SE China is an ideal site to study crustal recycling in association with subduction of the Paleo-Pacific Ocean (e.g., Wang et al., 2011; Zhou and Li, 2000). Although previous studies have reported preliminary results from petrology, mineralogy and geochemistry of the late Mesozoic mafic intrusions in this region (e.g., Dong et al., 1997; Li et al., 2012; Li et al., 2014; Wang, 2002; Xu et al., 1999; Zhao et al., 2004), systematic and detailed studies on these rocks are still lacking. First, the ages of the mafic intrusions have been dated by different methods such as $^{40}Ar/^{39}Ar$, Sm-Nd isochrons and zircon U-Pb isotope systems, which yield quite variable ages even for a single intrusion (e.g., Chen et al., 2007; Dong et al., 1997; Li et al., 2012; Wang and Lu, 1999). Second, there lack geochemical data (e.g., mineral-scale isotopes and whole-rock Pb-Hf isotopes) that help to evaluate the effect of open-system magmatic evolution. Third, regardless of variable degrees of crystal accumulation in these mafic intrusions (Li et al., 2012; Xu et al., 1999; Zhao et al., 2004), the previous studies have been focused on their whole-rock geochemical data instead of the parental magma compositions estimated from the equilibrium distribution of elements between the minerals and cumulate rocks (Bédard, 1994). Fourth, it remains debatable whether the "crust-like" isotopic signatures of the mafic intrusions were inherited from the mantle source or a result of open-system magmatic evolution (Dong et al., 1997; Li et al., 2012; Li et al., 2018; Wang, 2002). Finally, it is still poorly constrained about the thermal structure of the late Mesozoic subduction zone.

In this paper, we present a comprehensive study including petrology, mineralogy (in-situ analyses on mineral-scale chemical and isotopic compositions) and whole-rock geochemistry (major, trace element and Sr-Nd-Pb-Hf isotopic compositions) on three early Cretaceous mafic intrusions from the coastal region of SE China. This new dataset enables us to estimate the compositions and nature of the parental magmas and provide further insights into the predominant enrichment processes operating in the mantle wedge. By integrating with the previous data, we can outline the architecture of the Paleo-Pacific subduction zone beneath the SE China.

2. Geologic backgrounds and petrography

The South China Block (SCB) consists of two Precambrian blocks: the Yangtze Block in the northwest and the Cathaysia Block in the southeast, both of which were amalgamated along the Jiangnan Orogen during the Neoproterozoic (Fig. 1a, Zhang et al., 2013). A striking feature of SCB is that the Mesozoic igneous rocks are widely distributed in the Cathaysia Block. Felsic magmatism is volumetrically predominant (> 90%), with minor mafic-intermediate rocks (Zhou et al., 2006). Several large-scale NNE-trending sinistral faults are developed in this block. One of them is the Changle-Nan'ao fault that formed during the

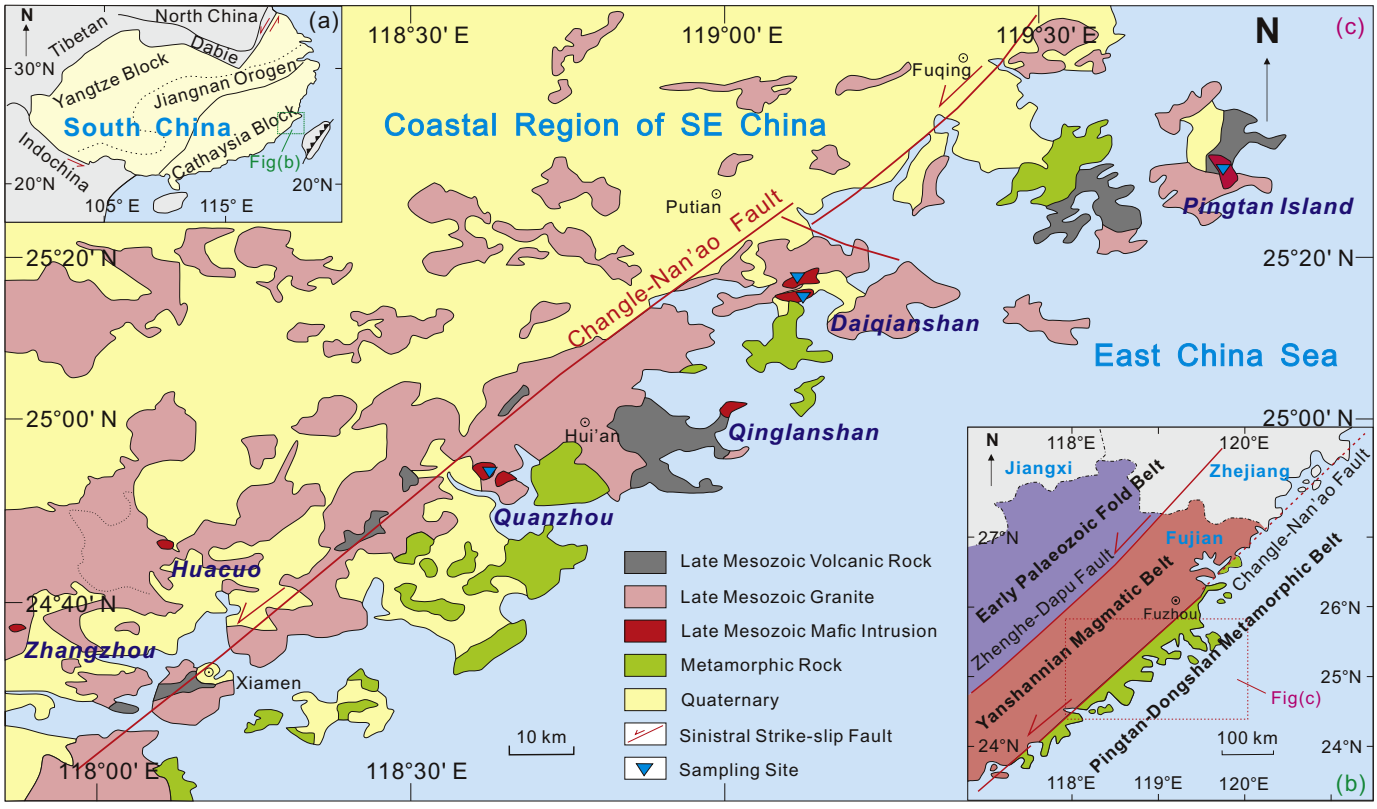

Fig. 1. A simplified tectonic map of South China (a, after Zhang et al., 2013), a sketch map of the coastal region in SE China (b, after Li et al., 2012) and the distribution of early Cretaceous mafic intrusions in the study area (c, after Li et al., 2012).

Cretaceous (Mao et al., 2014). Along this fault, the coastal region can be further divided into two tectonic units: the Yanshanian magmatic belt (predominant granite and rhyolite) in the west and the Pingtan-Dongshan metamorphic belt (pre-Mesozoic migmatitic gneiss and pelitic schist) in the east (Fig. 1b, Chen et al., 2002). A few Cretaceous mafic intrusions are sporadically distributed along this fault. From NE to SW, the Cretaceous mafic intrusions outcrop at Pingtan Island, Daiqianshan, Qinglanshan, Quanzhou, Huacuo and Zhangzhou (Fig. 1c). Except for the Qinglanshan pluton that intrudes into the Mesozoic volcanic lavas, the rest of mafic intrusions show close association with the late Mesozoic granitoids, forming bimodal intrusive complexes along the coastal region of SE China (Li et al., 2012).

Here we select three mafic intrusions (Pingtan, Daiqianshan and Quanzhou), which are linearly distributed within the eastern belt, to conduct a comprehensive petrologic and geochemical study. All these mafic intrusions are hornblende gabbros in lithology (Fig. 2). Their petrographic features are described below:

The hornblende gabbro from Pingtan Island outcrops near the center of the complex in form of stock, surrounded by the synplutonic dikes and a few quenched enclaves within the granitoids (Xu et al., 1999). It is black in colour and medium- to coarse-grained, consisting mainly of plagioclase (50–65%), hornblende (25–40%), clinopyroxene (<10%) and accessory minerals such as magnetite, apatite, titanite and zircon. Plagioclase (0.2–2 mm) is generally euhedral to subhedral and display twinning and zoning. Hornblende is usually subhedral to anhedral (0.2–3 mm) with plagioclase inclusions in some crystals. Previous zircon U-Pb dating results yielded an emplacement age range from 115 ± 1 Ma to 117 ± 3 Ma (Dong et al., 1997; Li et al., 2018).

The hornblende gabbro from Daiqianshan occurs as a layered mafic intrusion. It is generally oval on the flat surface and occupies an area of ~3.5 km^2. The rock is also black in colour and fine- to medium-grained. Major minerals are plagioclase (45–60%) and hornblende (30–50%), with very few clinopyroxene (<5%). And accessary minerals are including magnetite, apatite, titanite and zircon. Plagioclase (0.1–1 mm) is euhedral to subhedral in shape and some crystals display twinning due to exsolution. Hornblende is subhedral to anhedral (0.2–2 mm) with some plagioclase inclusions. Previous studies obtained a whole-rock-mineral Sm-Nd isochron age of 95 ± 2 Ma (Wang and Lu, 1999), whereas the hornblende yielded an $^{40}Ar/^{39}Ar$ plateau age of 125.1 ± 2.3 Ma (Chen et al., 2007).

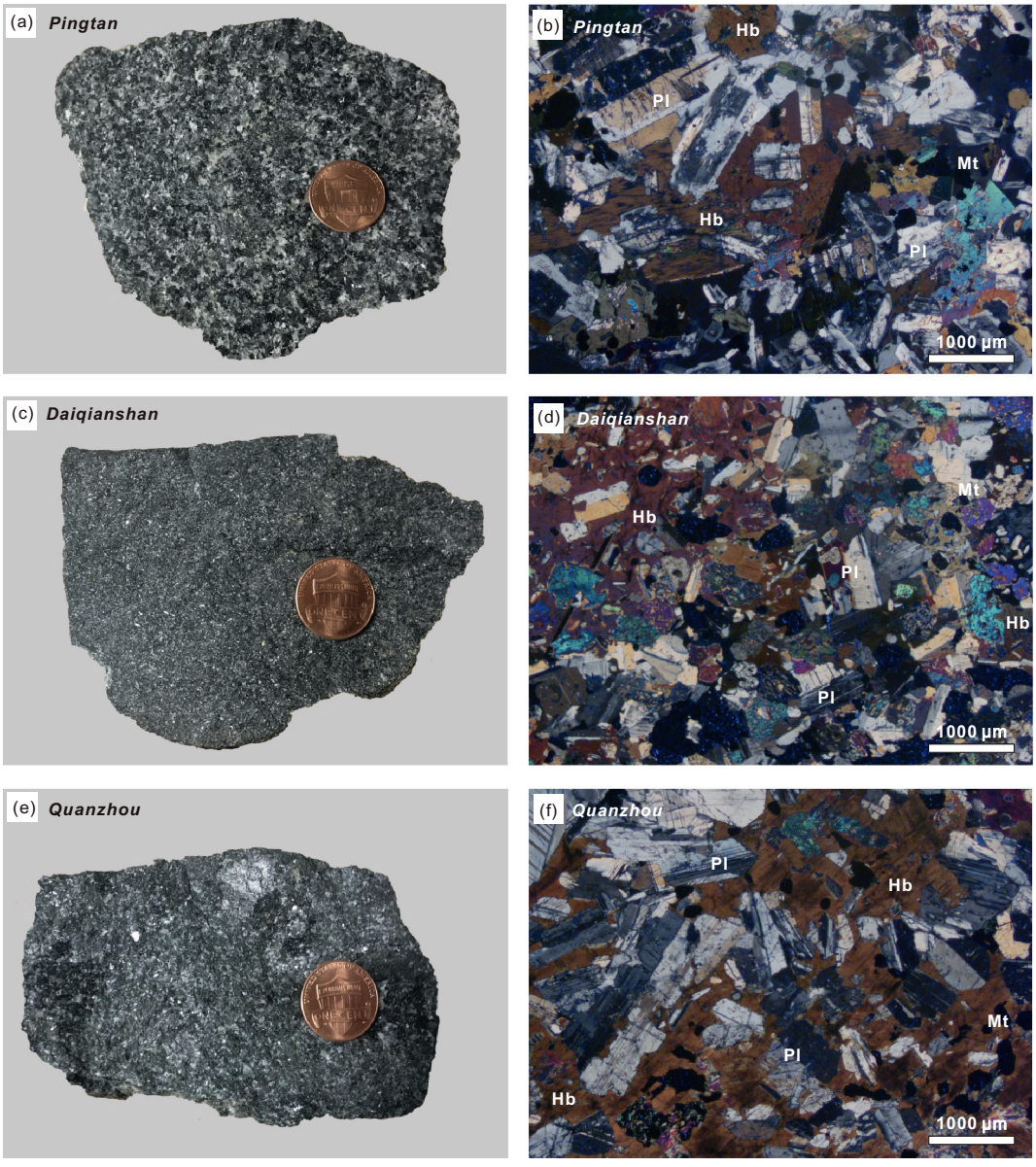

Fig. 2. Photos and corresponding micrographs of the Pingtan, Daiqianshan and Quanzhou mafic intrusions. Mineral abbreviations: Hb-hornblende; Pl-plagioclase; Mt-magnetite.

The hornblende gabbro from Quanzhou is located at Dongyueshan and Taohuashan. It outcrops in the form of stock. The samples are dark in colour and medium- to coarse-grained. Rock-forming minerals are dominated by plagioclase (50–60%) and hornblende (30–45%), with a small amount of clinopyroxene (<10%). Accessory minerals consist mainly of magnetite, apatite, titanite and zircon. Plagioclase (0.2–2 mm) is euhedral to subhedral and shows a twinning texture. Hornblende is subhedral to anhedral (0.5–5 mm) in shape with some containing plagioclase inclusions. Previous studies yielded a zircon U-Pb age range from 106.2 ± 1.2 Ma to 109 ± 1 Ma (Li et al., 1995; Li et al., 2012).

The petrographic observations indicate crystallization of plagioclase prior to hornblende in these three mafic intrusions. A summary of petrological and geochemical features of these mafic intrusions is presented in Table 1.

3. Analytical techniques

3.1. Zircon U-Pb dating

Zircon from the samples was separated by a sequence of procedures including crushing, sieving, magnetic/heavy liquid separation and was further handpicked under the binocular microscopes. Then it was mounted in the epoxy resin discs with the zircon standards (Plešovice and Qinghu) and polished to make sure the flatness of exposed surface. Transmitted/reflected light and cathodoluminescence (CL) images were taken prior to the analysis in order to reveal the internal texture and choose the suitable test position. The mount was vacuum-coated with high-purity gold to reach <20 Ω resistance before SIMS analysis. U-Pb ages of zircon were determined using a high-resolution secondary ion mass spectrometer (HR-SIMS) Cameca IMS-1280 HR at the Institute of Geology and Geophysics (IGG), CAS. Analytical point is about 10 × 15 μm in size. Analyses of zircon standards were interspersed with unknown samples. U-Th-Pb isotope ratios of unknown samples were calibrated relative to the standard zircon Plěsovice ($^{206}Pb/^{238}U = 0.05369$, ~ 337.1 Ma, Sláma et al., 2008). Repeated analyses of the Qinghu zircon standard yielded a weighted mean $^{206}Pb/^{238}U$ age of 159.6 ± 1.8 Ma (MSWD = 0.16, 2σ, $n = 11$), which is consistent with its reported value (159.5 ± 0.2 Ma, Li et al., 2013). More detailed instrument description and analytical procedure were reported by Li et al. (2009). Data reduction was carried out using the Isoplot/Ex v. 3.00 program (Ludwig, 2003). Uncertainties on individual analyses are reported at a 1σ level, and the calculated Concordia ages are quoted with 95% confidence interval.

3.2. Mineral compositions

Major element analysis of minerals and back-scattered electron (BSE) images were carried out using a JEOL LIXA-8100 Electron Microprobe at the Guangzhou Institute of Geochemistry (GIG), CAS. The main operating conditions of instrumental analysis include accelerating voltage of 15 kV, beam current of 10 nA, and 1–2 μm spot diameter. The analytical errors were <2%. The data reduction was performed via the atomic number absorption-fluorescence (ZAF) correction procedure.

3.3. In-situ Sr-Pb isotope analyses on plagioclase

The thin sections were washed in an ultrasonic bath with dilute HNO_3 (<1%) and ultrapure water for 15 min before analysis, then dried with a nitrogen gas gun. In-situ Sr-Pb isotope analyses were carried out on a Neptune Plus Multi-Collector Inductively Coupled Plasma Mass Spectrometry (MC-ICP-MS, Thermo Scientific) equipped with a 193 nm laser ablation system (Resonetics) at the GIG-CAS. Before analysis, basaltic glass standards NKT-1G and BHVO-2G were measured to evaluate the accuracy of the instrument.

For in-situ Sr isotope analysis on plagioclase, the isotope signals were detected using Faraday cups under a static mode. Helium was chosen as the carrier gas (800 mL/min) and the main parameters of laser were set as follows: the diameter of laser beam ranges between 112 and 155 μm, the repetition rate is 6 Hz, and the energy density is ~ 4 J/cm^2. During the first 30s, the gas blank of the system was monitored under the circumstance with the laser beam off. In the following 30s, the signals of laser ablation on plagioclase were collected in the condition of laser beam on. The voltages of gas blank of ^{83}Kr and ^{88}Sr were <2.5 mV and 0.5 mV, respectively. Gas blank was subtracted from the raw time-resolved signal intensities in order to correct the interferences of ^{84}Kr and ^{86}Kr on ^{84}Sr and ^{86}Sr. Mass bias of $^{87}Sr/^{86}Sr$ was normalized to $^{86}Sr/^{88}Sr = 0.1194$ using an exponential law. The detailed data reduction procedure was described by Zhang et al. (2015). Repeated analyses of the external standard NKT-1G yielded a weighted $^{87}Sr/^{86}Sr$ value of 0.70351 ± 0.00007 (2SD, $n = 22$), which is consistent with the reference value (0.70351 ± 0.00002, Elburg et al., 2005).

For in-situ Pb isotope analysis, an X skimmer cone and an additional nitrogen gas with a flow rate of 2 mL/min were used to improve the instrumental sensitivity. Isotope signals were detected with ion counters in the static mode. Helium was chosen as the carrier gas (800 mL/min) and the main parameters of the laser were set as follows: the beam diameter ranges between 45 and 80 μm, the repetition rate is 6 Hz, and the energy density is ~4 J/cm^2. During the first 28s, the gas blank of the system was monitored under the circumstance with the laser beam off. In the following 30s, the signals of laser ablation on plagioclase were collected in the condition of laser beam on. Gas blank of ^{202}Hg and ^{208}Pb was subtracted from the raw time-resolved signal intensities during each cycle. The standard-sample-bracketing method (SSB) was used to correct the mass bias and instrumental drift. The detailed analytical method was reported in Zhang et al. (2014). Repeated analyses of the international basaltic glass BHVO-2G yielded mean

Table 1
A summary of petrological and geochemical features of early Cretaceous mafic intrusions in SE China.

Intrusion	Pingtan Island	Daiqianshan	Quanzhou
Lithology	Hornblende gabbro	Hornblende gabbro	Hornblende gabbro
Mineral assemblage	Cpx + Pl + Hb + Mt. + Ap + Ttn + Zr	Cpx + Pl + Hb + Mt. + Ap + Ttn + Zr	Cpx + Pl + Hb + Mt. + Ap + Ttn + Zr
An component in Pl	core:76–89, rim:35–61	82–95	75–92
T_{Hb} (°C)	761–893	846–924	775–922
P_{Hb} (MPa)	103–207	217–353	139–357
H_2O_{melt} (wt%)	4.47–5.52	5.85–7.57	5.09–7.25
Age (Ma)	115.8 ± 1.2	113.0 ± 2.0	113.3 ± 1.2
SiO_2 (wt%)	46.96–52.07	38.09–44.80	42.23–47.03
MgO (wt%)	5.17–7.17	5.06–8.24	6.08–7.70
$Mg^{\#}$	48.4–57.4	38.6–56.2	41.5–60.8
$(La/Yb)_N$	3.89–10.6	1.73–6.06	3.62–8.32
Eu/Eu*	0.91–1.19	0.90–1.18	0.82–1.15
Sr/Sr*	1.89–3.10	3.17–8.17	2.42–6.64
$^{87}Sr/^{86}Sr_{(i)}$	0.70536–0.70560	0.70591–0.70608	0.70542–0.70601
ε_{Nd} (t)	−0.4 ~ −1.6	−2.4 ~ −3.1	−2.4 ~ −2.9
ε_{Hf}(t)	+3.2 ~ +3.9	+0.5 ~ +1.4	+1.4 ~ +2.1
$^{206}Pb/^{204}Pb_{(i)}$	18.131–18.248	18.427–18.507	18.526–18.553
$^{208}Pb/^{204}Pb_{(i)}$	38.193–38.363	38.631–38.675	38.678–38.722
$^{207}Pb/^{204}Pb_{(i)}$	15.579–15.597	15.629–15.637	15.637–15.641
$^{87}Sr/^{86}Sr$ in Pl	0.70543–0.70564	0.70586–0.70602	0.70589–0.70609
$^{208}Pb/^{206}Pb$ in Pl	2.109–2.119	2.094–2.111	2.086–2.097
$^{207}Pb/^{206}Pb$ in Pl	0.858–0.864	0.844–0.851	0.842–0.846

Note: Mineral abbreviations are Cpx – clinopyroxene; Hb – hornblende; Pl – plagioclase; Mt. – magnetite; Ap – apatite; Ttn – titanite; Zr – zircon; An – anorthosite.
$Mg^{\#} = 100 \times Mg/(Mg + \sum Fe)$ in atomic ratio.
The subscript "N" denotes chondrite normalization.
$Eu/Eu^* = Eu_N/(Sm_N \times Gd_N)^{0.5}$.
$Sr/Sr^* = Sr_{PM}/(Ce_{PM} \times Nd_{PM})^{0.5}$, the subscript "PM" denotes primitive mantle normalization.
The initial isotope ratios are recalculated using the zircon U-Pb ages obtained in this study.

values of $^{208}Pb/^{206}Pb = 2.053 \pm 0.006$ (2SD, n = 22) and $^{207}Pb/^{206}Pb = 0.833 \pm 0.003$ (2SD, n = 22), which are consistent with the reported values (2.048 and 0.832, respectively) in Elburg et al. (2005).

3.4. Whole-rock major and trace element analyses

The samples for whole-rock geochemical analyses were firstly crushed to sort the fresh chips, which were then leached in 0.5 N HCl for 1 h and cleaned in purified water. After the weathered surfaces were removed, the chips were then powdered to <200 mesh for chemical analysis.

Major oxide contents were analyzed by wavelength X-ray fluorescence spectrometry (XRF) at Australian Laboratory Service (ALS) Group. In the beginning, ~0.5 g sample powder was mixed with 3.6 g $Li_2B_4O_7$, 0.4 g LiF, 0.3 g NH_4NO_3, and minor LiBr in a platinum crucible. Then it was melted in a furnace to form a glass disk for major element analysis. The analytical errors were <1%. Trace element concentrations of the samples were determined by a Perkin-Elmer ELAN 6000 inductively coupled plasma mass spectrometry (ICP-MS) after acid digestion in high-pressure Teflon bombs at the GIG-CAS. During the course, ~ 50 mg sample powder was mixed with 1 mL of HF and 0.5 mL of HNO_3 in a Teflon cup. Then the Teflon cup was sealed in a stainless steel bomb and heated at 190 °C for 48 h. More detailed analytical procedure was reported by Liu et al. (1996). The analytical errors were <5% for rare earth element (REE) and high field strength element (HFSE), and 5–10% for the other elements, based on repetitive analyses of USGS standards GSR-1 (granite), GSR-2 (andesite) and GSR-3 (basalt).

3.5. Whole-rock Sr-Nd-Pb-Hf isotope analyses

Whole-rock Sr-Nd-Pb-Hf isotope compositions of the samples were measured on a Neptune Plus MC-ICP-MS at the GIG-CAS.

Detailed analytical procedures of Sr and Nd isotope were described by Li et al. (2006). Sr and REE were separated via cation columns, and Nd fractions were further separated by HDEHP-coated Kef columns. The procedural blanks were <200 pg for Sr and about 30 pg for Nd. The measured values of $^{87}Sr/^{86}Sr$ and $^{143}Nd/^{144}Nd$ were separately normalized to $^{86}Sr/^{88}Sr = 0.1194$ and $^{146}Nd/^{144}Nd = 0.7219$. $^{87}Sr/^{86}Sr$ and $^{143}Nd/^{144}Nd$ ratios of the samples were corrected to the NBS SRM 987 standard ($^{87}Sr/^{86}Sr = 0.710247 \pm 8$, 2σ) and the Shin Etsu JNdi-1 standard ($^{143}Nd/^{144}Nd = 0.512115 \pm 4$, 2σ), respectively. Repeated analyses of NBS SRM 987 standard and the Shin Etsu JNdi-1 standard separate yielded mean values of 0.710248 ± 10 and 0.512114 ± 6 (2σ, $n = 6$).

For Pb isotopic analysis, the sample powder in the Teflon beakers were spiked and dissolved in concentrated HF at the temperature of 180 °C for 7 h. Then Pb was separated via the cation-exchange technique with diluted HBr. The procedural blanks were <50 pg Pb. Repeated analyses of SRM 981 yielded mean values of $^{206}Pb/^{204}Pb = 16.935 \pm 0.0006$, $^{207}Pb/^{204}Pb = 15.490 \pm 0.0006$ and $^{208}Pb/^{204}Pb = 36.692 \pm 0.0015$ (2σ, n = 6), in agreement with the corresponding isotopic values reported by Todt et al. (1996).

For the Hf isotope determination, fraction of Hf was separated via a modified single-column separation procedure including ion exchange with Ln-Spec resin. More detailed analytical procedure was reported by Li et al. (2005). The procedural blanks were about 50 pg for Hf. The values of $^{176}Hf/^{177}Hf$ ratios were normalized to $^{179}Hf/^{177}Hf = 0.7325$. During the analyses, the reported $^{176}Hf/^{177}Hf$ ratios were adjusted to the standard sample of JMC-14374 (0.282188 ± 0.000005, 2σ). Repeated analyses of JMC-14374 yielded a mean value of 0.282187 ± 0.000005 (2σ, n = 6).

During the whole-rock Sr-Nd-Pb-Hf isotope analyses, the USGS reference BHVO-2 yielded $^{87}Sr/^{86}Sr = 0.703475 \pm 8$ (2σ, n = 6), $^{143}Nd/^{144}Nd = 0.512981 \pm 5$ (2σ, n = 6), $^{206}Pb/^{204}Pb = 18.6513 \pm 6$ (2σ, n = 6), $^{207}Pb/^{204}Pb = 15.5373 \pm 6$ (2σ, n = 6) and $^{208}Pb/^{204}Pb = 38.2400 \pm 13$ (2σ, n = 6) and $^{176}Hf/^{177}Hf = 0.283093 \pm 4$ (2σ, n = 6), respectively, being in agreement with recommended values reported in Weis et al. (2005). Analytical errors for the Sr-Nd-Pb-Hf isotope data are given as 2σ.

4. Results

4.1. Zircon U-Pb geochronology

The results of SIMS zircon U-Pb dating for the three mafic intrusions are listed in Appended Table S1. Zircon grains from the Pingtan intrusion (17PT-1) are transparent in colour, and mostly lath-shaped whereas some others show oscillatory zoning. The zircon grains range from 30 × 50 μm to 50 × 150 μm with a wide length/width ratio variation of 2–6. Th/U ratios of the zircon range from 0.84 to 1.44. A total of thirteen analyses yield ages ranging from 113.3 ± 2.3 Ma to 119.5 ± 2.1 Ma, with a mean $^{206}Pb/^{238}U$ age of 115.8 ± 1.2 Ma (MSWD = 0.72, 2σ, Fig. 3a). This age is similar to the previous dating results (Dong et al., 1997; Li et al., 2018), confirming the emplacement during early Cretaceous.

Zircons crystals from the Daiqianshan intrusion (17DQS-1) are also transparent. The zircon crystals vary from 20 × 30 μm to 40 × 100 μm with a length/width ratio of 1–3. They have a Th/U ratio of 0.61–1.46. Nine analyses of these zircon crystals yield an average concordant $^{206}Pb/^{238}U$ age of 113.0 ± 2.0 Ma (MSWD = 2.1, 2σ, Fig. 3b). The obtained zircon U-Pb age is much younger than the previous hornblende Ar-Ar plateau age but is older than the Sm-Nd isochron age (Chen et al., 2007; Wang and Lu, 1999). Instead, this new age is similar to that of the Pingtan gabbro, indicating the emplacement during early Cretaceous.

Zircon grains separated from the Quanzhou intrusion (17QZ-1) are mostly translucent. The zircon crystals range from 20 × 20 μm to 35 × 100 μm with a narrow length/width ratio of 1–3. Th/U ratio varies between 0.61 and 2.24. The average $^{206}Pb/^{238}U$ age of nine zircon grains is 113.3 ± 1.2 Ma (MSWD = 1.08, 2σ, Fig. 3c). This age is identical to that of the Daiqianshan intrusion.

Compared with the previous studies that suggested the emplacement of mafic magmas during 125 Ma to 95 Ma (Chen et al., 2007; Wang and Lu, 1999), our new zircon U-Pb age analyzed by SIMS yield a narrow age range between 116 Ma and 113 Ma for the three mafic intrusions, confirming an extensive mafic magmatism during early Cretaceous.

4.2. Mineral chemistry and Sr-Pb isotopes of plagioclase

4.2.1. Hornblende

The chemical compositions of hornblende for all samples are listed in Appended Table S2, and the classification and P-T-H_2O conditions are shown in Fig. 4.

Hornblende from the Pingtan intrusion is dominated by magnesiohornblende with minor tschermakite. Thermodynamic calculation results show that it was formed in an environment with T = 761–893 °C, P = 103–207 MPa, H_2O_{melt} = 4.47–5.52 wt%.

Hornblende from the Daiqianshan intrusion consists of magnesiohastingsite and edenite. Thermodynamic calculation results suggest its crystallization in the conditions of T = 846–924 °C, P = 217–353 MPa, H_2O_{melt} = 5.85–7.57 wt%.

Hornblende from the Quanzhou intrusion consists of magnesiohornblende and tschermakite. Thermodynamic calculation suggests that it crystallized in the conditions of T = 775–922 °C, P = 139–357 MPa, H_2O_{melt} = 5.09–7.25 wt%.

In summary, the hornblende from the intrusions belongs to calcic amphibole (Fig. 4a-b). It crystallized in water-rich magmas (4.47–7.57 wt%) at low pressure (103–357 MPa), corresponding to upper crustal levels (Fig. 4c-d).

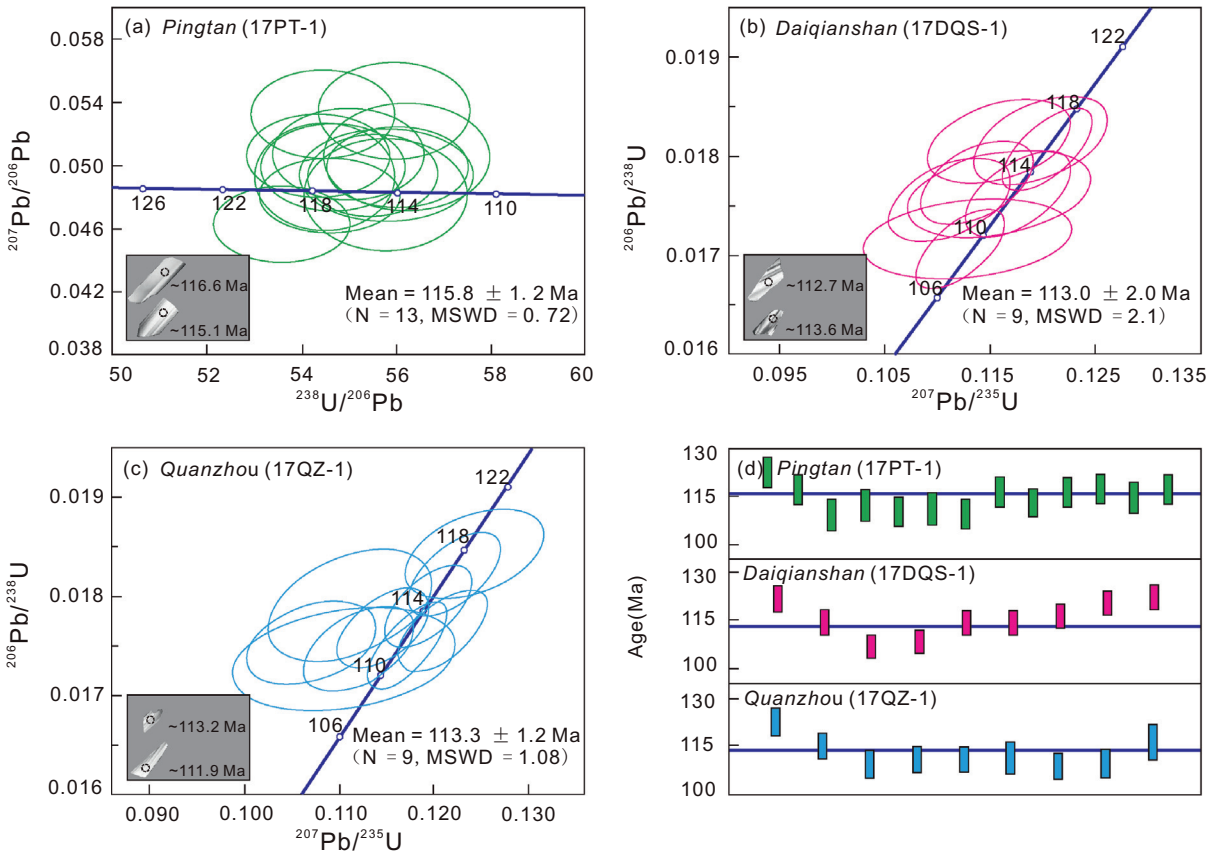

Fig. 3. Zircon U-Pb Concordia diagrams of the early Cretaceous mafic intrusions.

4.2.2. Plagioclase

The chemical compositions of plagioclase for all samples are listed in Appended Table S3. As is shown in Fig. 5, plagioclase from the Pingtan intrusion contain a Ca-rich core (An_{76} ~ An_{89}) overgrown by a Na-rich rim (An_{35} ~ An_{61}). In addition, there exist microcracks in the cores, which are filled by Na-rich plagioclase. Such structural and compositional variations in plagioclase is resulted from rapid decompression and subsequent degassing/cooling of the magma (e.g., Nelson and Montana, 1992). In contrast with the obvious compositional variations in plagioclase from the Pingtan intrusion, the plagioclase crystals from the Daiqianshan (An_{82} ~ An_{95}) and Quanzhou (An_{75} ~ An_{92}) plutons show relatively narrow compositional ranges (Fig. 5). Accordingly, the plagioclase from the three intrusions is marked by high calcic component.

4.2.3. Fe-Ti oxides

The chemical compositions of Fe-Ti oxides for all samples are listed in Appended Table S4. The Fe-Ti oxides are magnetite, which has a TiO_2 range of 0.01–0.71 wt%, 0.05–0.13 wt% and 0.07–0.18 wt%, respectively for the Pingtan, Daiqianshan and Quanzhou intrusions.

4.2.4. In-situ Sr-Pb isotopes of plagioclase

In-situ Sr and Pb isotopes of plagioclase are listed in Appended Table S5 and S6, respectively. The measured $^{87}Sr/^{86}Sr$ ratios in plagioclase exhibit a rather narrow variation (Fig. 6a). To be specific, a total of thirty-three Sr isotope analyses on plagioclase from the Pingtan intrusion (17PT-1) yield a range from 0.70543 ± 0.00009 to 0.70564 ± 0.00005. Seventeen Sr isotope analyses on plagioclase grains from the Daiqianshan intrusion (17DQS-1) show an $^{87}Sr/^{86}Sr$ range from 0.70586 ± 0.00006 to 0.70602 ± 0.00007. Fourteen Sr isotope analyses on plagioclase from the Quanzhou intrusion (17QZ-1) give an $^{87}Sr/^{86}Sr$ range between 0.70589 ± 0.00007 and 0.70609 ± 0.00006. Considering the analytical errors, the measured Sr isotope ratios within a single plagioclase crystal and among different plagioclase crystals are similar or even identical to the whole-rock Sr isotope ratios from each intrusion. Regardless of the compositional variation in plagioclase as observed in the Pingtan intrusion, there lacks a clear correlation between the An content and $^{87}Sr/^{86}Sr$ of plagioclase in a single intrusion (Appended Fig. S1).

Similar to the in-situ Sr isotope data, the plagioclase crystals also have similar or identical Pb isotope compositions to the whole-rock samples of each mafic intrusion. The $^{207}Pb/^{206}Pb$ and $^{208}Pb/^{206}Pb$ ratios of plagioclase from the Pingtan intrusion (17PT-1) yield ranges of 0.858 ± 0.001–0.864 ± 0.001 and 2.109 ± 0.002–2.119 ± 0.002, respectively. The Pb isotopic compositions of plagioclase from the Daiqianshan intrusion (17DQS-1) yield a $^{207}Pb/^{206}Pb$ range of 0.844 ± 0.001–0.851 ± 0.001 and a $^{208}Pb/^{206}Pb$ range of 2.094 ± 0.003–2.111 ± 0.003. The plagioclase from the Quanzhou intrusion (17QZ-1) show a $^{207}Pb/^{206}Pb$ range between 0.842 ± 0.001 and 0.846 ± 0.001 and a $^{208}Pb/^{206}Pb$ range between 2.082 ± 0.001 and 2.097 ± 0.003, respectively. As shown in Fig. 6b, the Pb isotopes of plagioclase display a mixing trend between a depleted mantle (DM) and a subducted sediment component.

4.3. Whole-rock major and trace elements

The results of major oxide (wt%) and trace element (ppm) contents of the representative samples are listed in Appended Table S7. The early Cretaceous mafic intrusions in SE China show large compositional ranges, e.g., a SiO_2 range of 38.1–52.1 wt%, a MgO range of 5.1–8.2 wt %, a $Fe_2O_3^T$ range of 9.2–21.3 wt%, a CaO range of 9.0–14.4 wt%, a Al_2O_3 range of 13.5–22.1 wt%, a TiO_2 range of 0.7–2.3 wt% and a $Mg^{\#}$ ($Mg^{\#}$ = 100 Mg/(Mg + ∑Fe) in atomic ratio) range of 38.6–60.8. They

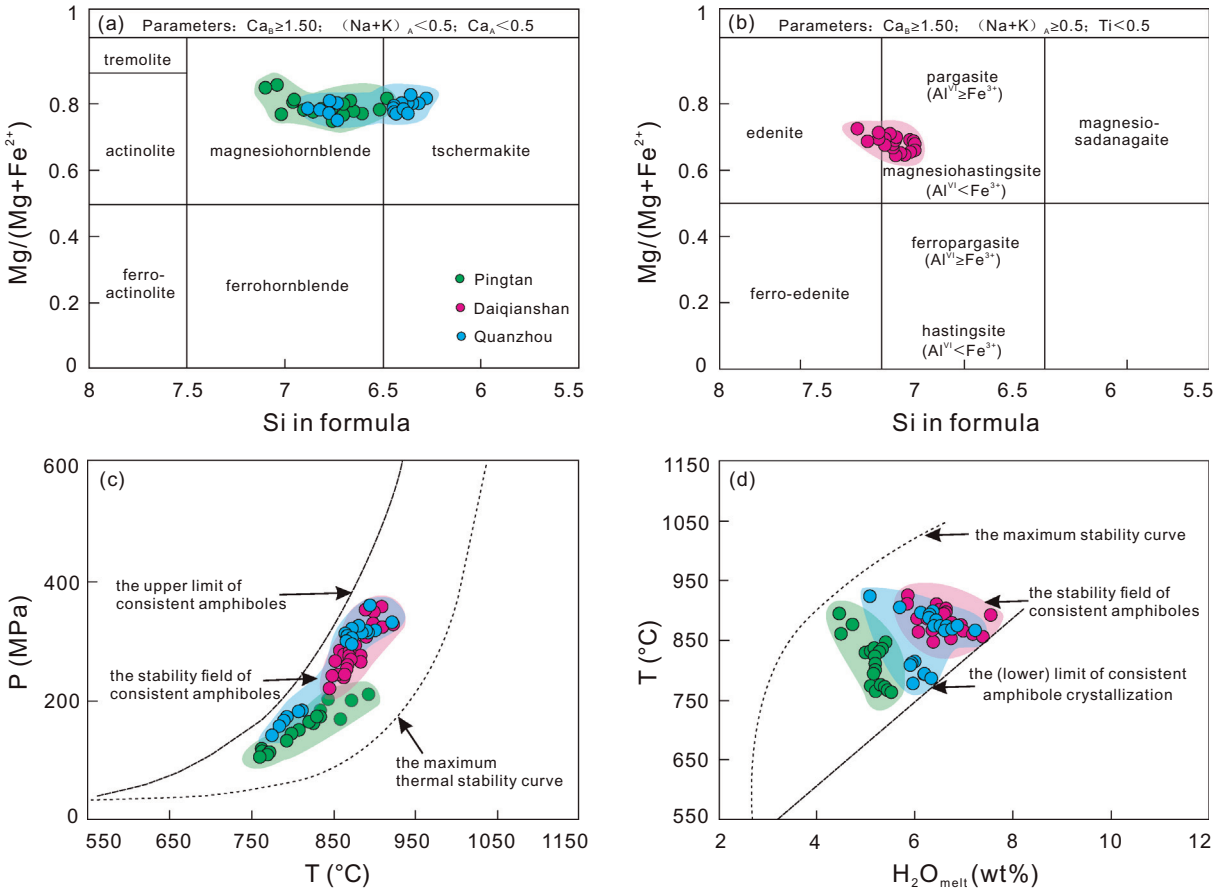

Fig. 4. Classification diagrams of calcic amphiboles in $Mg/(Mg + Fe^{2+})$ versus Si in formula (a and b, after Hawthorne and Oberti, 2006), T versus P (c) and H_2O_{melt} versus T(d) correlations. The thermodynamic calculation method was described in Ridolfi and Renzulli (2012).

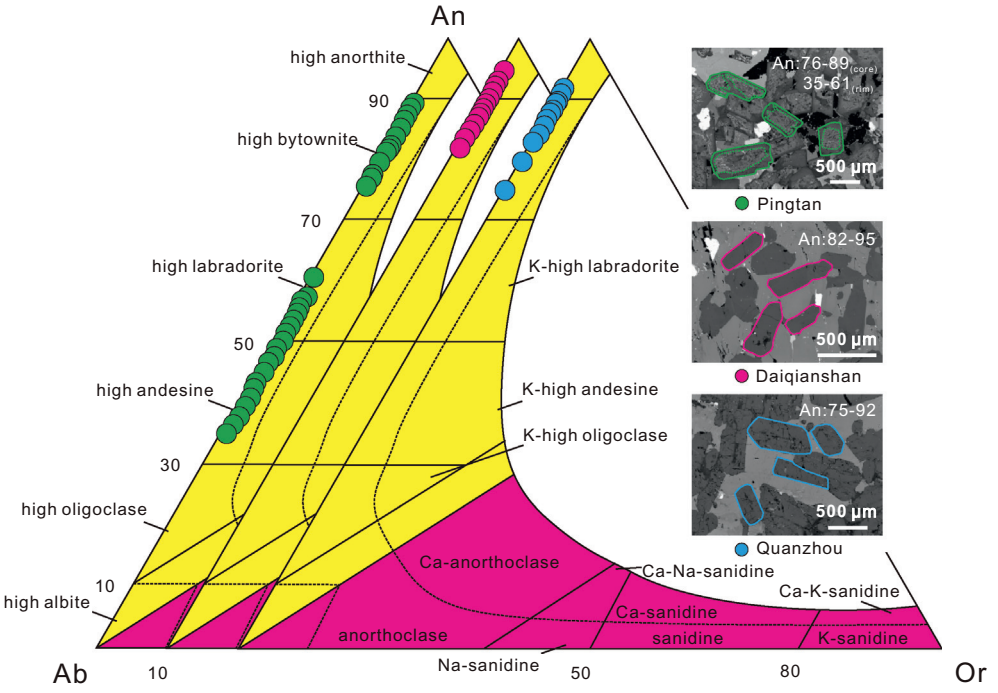

Fig. 5. A classification diagram of plagioclase (modified after Parsons, 2010).

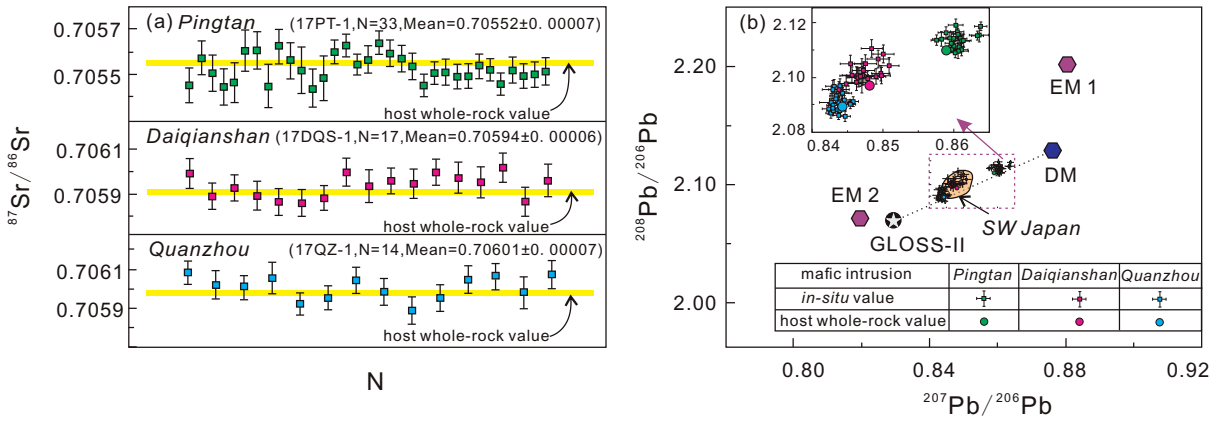

Fig. 6. In-situ analysis of Sr and Pb isotopes in plagioclase from the mafic intrusions in SE China. Data sources: DM, EM1, and EM2 (Iwamori and Nakamura, 2015); GLOSS-II (Plank, 2014); High-Mg andesites in the SW Japan arc (Shimoda et al., 1998; Tatsumi et al., 2003).

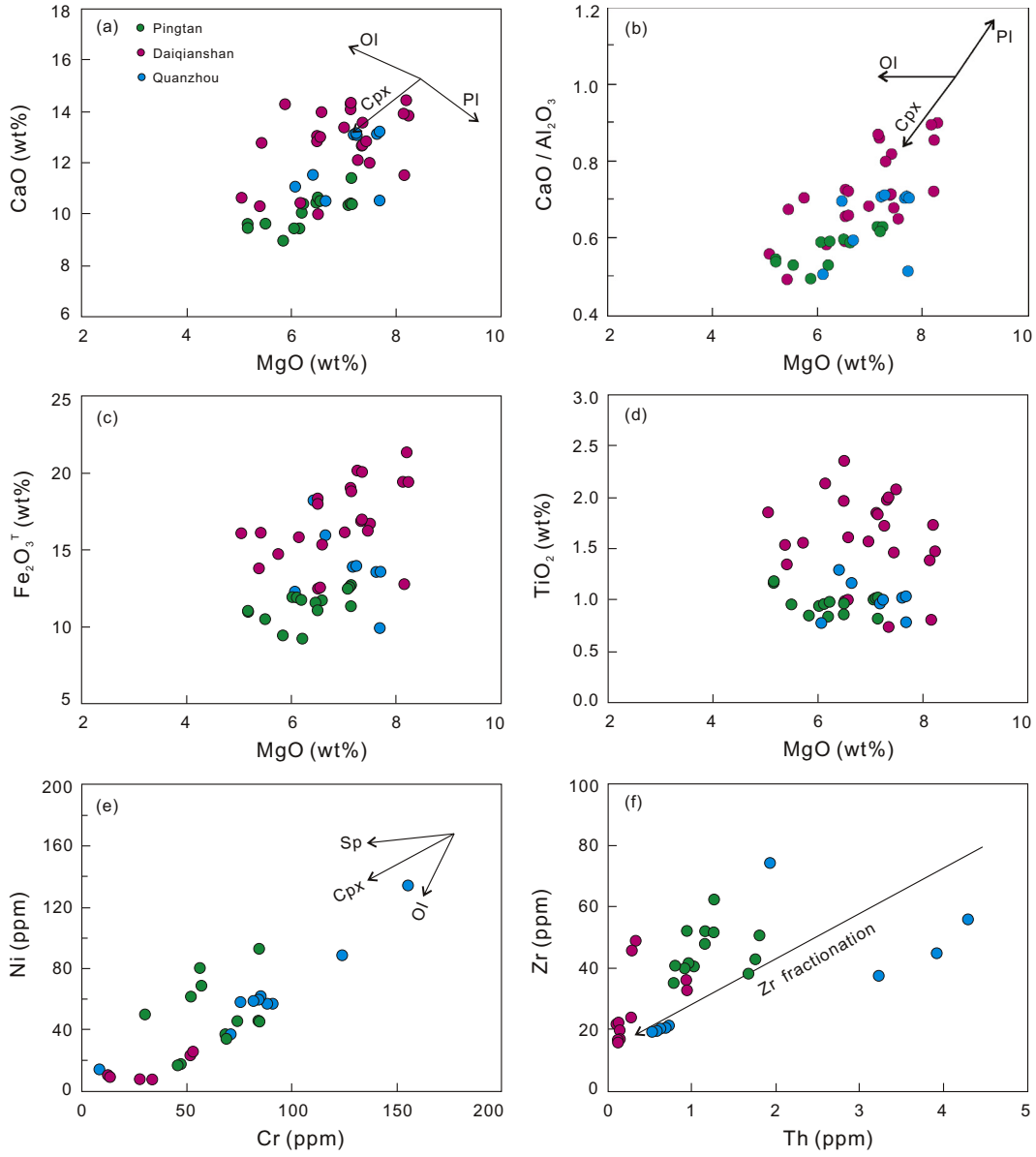

Fig. 7. Diagrams show the covariant relationships among major oxides, trace elements and elemental ratios of the early Cretaceous mafic intrusions. (a) MgO versus CaO, (b) MgO versus CaO/Al_2O_3, (c) MgO versus $Fe_2O_3^T$, (d) MgO versus TiO_2, (e) Cr versus Ni, (f) Th versus Zr. Data sources: Pingtan (Li et al., 2018; Xu et al., 1999 and this study); Daiqianshan (Wang, 2002; Xu et al., 1999; Zhao et al., 2004 and this study); Quanzhou (Li et al., 2012 and this study).

generally have low to medium K_2O contents (0.1–1.1 wt%) with an average of 0.4 wt%. These rocks show broad positive correlations of MgO with CaO and CaO/Al_2O_3 (Fig. 7a-b). Compared with the other two mafic intrusions, samples from the Daiqianshan pluton generally have higher TiO_2 contents (Fig. 7d). In addition, there exist positive relationships between Cr and Ni and between Th and Zr for most samples within each mafic intrusion (Fig. 7e-f).

In the chondrite-normalized REE patterns (Fig. 8a, c and e), these mafic rocks are characterized by variable enrichment in light REEs and depletion in heavy REEs with variable $(La/Yb)_N$ ratios (the subscript N denotes chondrite normalization, $(La/Yb)_N$= 3.89–10.61, 1.73–6.06 and 3.62–8.32 respectively from the Pingtan, Daiqianshan and Quanzhou intrusions). They also show variable Eu anomalies, with Eu/Eu^* = 0.91–1.19, 0.90–1.18 and 0.82–1.15, respectively for the three intrusions. Some samples from the Daiqianshan intrusion display convex REE patterns with middle REE (e.g., Nd) enrichment that is typical of hornblende accumulation.

In the primitive mantle-normalized trace element spidergrams (Fig. 8b, d and f), all samples show variable enrichment in large ion lithophile elements (LILEs, such as Ba, K and Sr) and light REEs, with variable depletion in HFSEs relative to neighboring REEs. Consistent with the plagioclase accumulation, all samples have positive Sr anomalies (Sr/Sr^* =1.89–8.17). In addition, some samples from the Daiqianshan and Quanzhou intrusions even show positive Ti anomalies, in agreement with the hornblende accumulation. There also exists an obvious synchronous fluctuation of Th-U with Zr-Hf in the Daiqianshan and Quanzhou mafic intrusions (Fig. 8d and f), whereas such a fluctuant feature is weak in the Pingtan intrusion.

4.4. Whole-rock Sr-Nd-Pb-Hf isotopes

Whole-rock Sr-Nd-Pb-Hf isotope compositions of representative samples from the Pingtan, Daiqianshan and Quanzhou intrusions are presented in Appended Table S8. The initial ratios of isotopes ($^{87}Sr/^{86}Sr_{(i)}$, $\varepsilon_{Nd}(t)$, $^{206}Pb/^{204}Pb_{(i)}$, $^{207}Pb/^{204}Pb_{(i)}$, $^{208}Pb/^{204}Pb_{(i)}$ and $\varepsilon_{Hf}(t)$) are recalculated by using the zircon U-Pb ages obtained in this study.

The samples collected within a single intrusion generally show narrow Sr-Nd-Pb-Hf isotopic variations. Samples from the Pingtan intrusion have $^{87}Sr/^{86}Sr_{(i)}$ = 0.70536–0.70560, $\varepsilon_{Nd}(t)$ = −0.4 ~ −1.6, $^{206}Pb/^{204}Pb_{(i)}$ = 18.13–18.25, $^{207}Pb/^{204}Pb_{(i)}$ = 15.58–15.60, $^{208}Pb/^{204}Pb_{(i)}$ = 38.19–38.36 and $\varepsilon_{Hf}(t)$ = +3.2 ~ +3.9. Relative to the Pingtan intrusion, the samples from the Daiqianshan and Quanzhou intrusions have similar but a little more evolved Sr-Nd-Pb-Hf isotopic

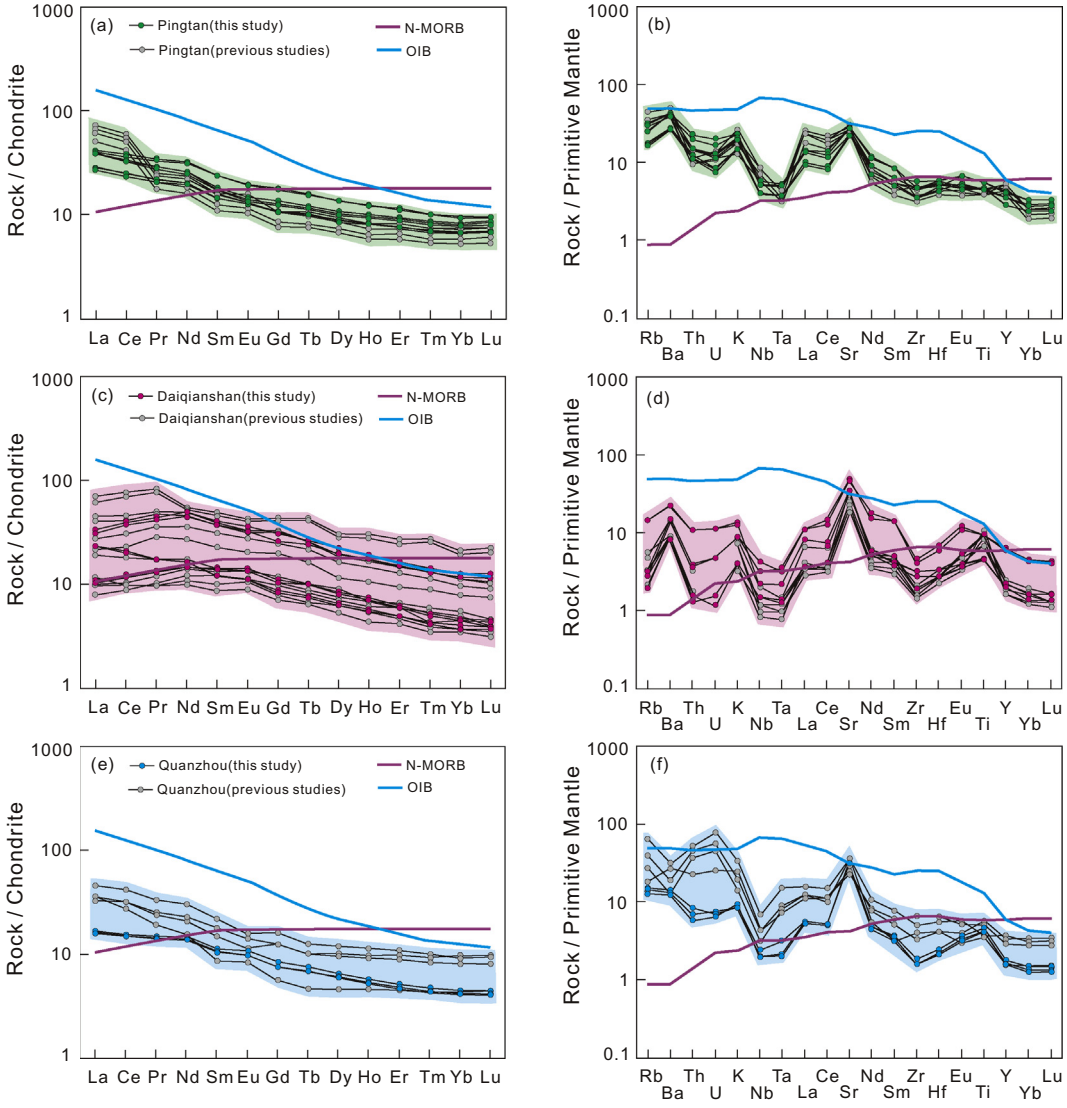

Fig. 8. Chondrite-normalized REE patterns (left) and trace element spider diagrams (right) of the mafic intrusions. Data sources: normalized values of chondrite and primitive mantle and data for OIB and N-MORB are from Sun and McDonough (1989); the others are the same as in Fig. 7.

compositions, with $^{87}Sr/^{86}Sr_{(i)}$ = 0.70542–0.70609, $\varepsilon_{Nd}(t)$ = −2.4 ~ −3.1, $^{206}Pb/^{204}Pb_{(i)}$ = 18.48–18.55, $^{207}Pb/^{204}Pb_{(i)}$ = 15.63–15. 64, $^{208}Pb/^{204}Pb_{(i)}$ = 38.63–38.72 and $\varepsilon_{Hf}(t)$ = +0.5 ~ +2.1. The Sr-Nd-Pb-Hf isotopic compositions are essentially similar to those arc magmas from SW Japan (Fig. 9).

5. Discussion

5.1. Magmatic evolution

Most mafic rocks experience complex magmatic evolution such as fractional crystallization, accumulation, wall-rock assimilation or contamination and magma mixing. These processes exert important effects on the compositional and isotopic variations and make it difficult to investigate the origin of mafic magmas. In the following, we will discuss the possible influence of magmatic evolution in these early Cretaceous mafic intrusions in SE China.

5.1.1. Crustal contamination or AFC processes

Crustal contamination or AFC processes may lead to an increase of whole-rock $^{87}Sr/^{86}Sr_{(i)}$ and a decrease of $\varepsilon_{Nd}(t)$ following the magmatic evolution. Although the mafic rocks show highly variable SiO_2, $Mg^{\#}$, Sr and Nd concentrations and Nb/La ratios, weak variations in the whole-rock $^{87}Sr/^{86}Sr_{(i)}$ and $\varepsilon_{Nd}(t)$ of each intrusion are observed, precluding a significant role of crustal contamination or assimilation (Fig. 10a–f).

In the early Cretaceous mafic intrusions, plagioclase is an early crystallizing phase and experiences subsolidus exsolution during cooling, so it witnesses the complete magmatic evolution. The in-situ Sr isotope analyses on plagioclase also yield weak $^{87}Sr/^{86}Sr$ variations, with the mean $^{87}Sr/^{86}Sr$ ratio at 0.7055, 0.7059 and 0.7060, respectively for the Pingtan, Daiqianshan and Quanzhou intrusions (Fig. 6). The average Sr isotope ratio for each intrusion is almost identical to the whole-rock $^{87}Sr/^{86}Sr_{(i)}$, indicating negligible addition of exotic radiogenic Sr from the wall rocks. Similarly, the in-situ Pb isotope analyses on plagioclase also rule out a significant addition of radiogenic Pb from the wall rocks.

Collectively, both the whole-rock geochemical data and in-situ Sr and Pb isotope compositions of plagioclase indicate a close-system magmatic evolution for the mafic intrusions, during which the role of crustal contamination or assimilation was minor.

5.1.2. Fractional crystallization and accumulation

The mafic intrusions in SE China show positive correlations of CaO and CaO/Al_2O_3 with MgO and Cr versus Ni (Fig. 7a–b and e), indicating a significant role of fractional crystallization of ferromagnesian minerals such as olivine and clinopyroxene. In addition, some samples show weakly negative Eu anomalies in chondrite-normalized REE patterns (Fig. 8a, c and e), suggesting a role of plagioclase fractionation. Finally, the positive relationship between Th and Zr (Fig. 7f) suggest the fractionation of zircon, consistent with the synchronous fluctuation in Zr-Hf and Th-U in the PM-normalized spidergrams (Fig. 8b, d and f).

Compared with the role of fractional crystallization, the effect of crystal accumulation is more evident in these mafic intrusions. The facts that all samples show positive Sr anomalies in the trace element spidergrams and most of them have positive Eu anomalies in REE patterns (Fig. 8) indicate the effect of plagioclase accumulation. Although hornblende is a later crystallizing mineral, its accumulation may be responsible for the low SiO_2 and high TiO_2 in some samples, in particular those from the Daiqianshan intrusion, which also have lower contents of LILEs and enriched middle REE (e.g., Nd and Sm) patterns (Fig. 8, Guo et al., 2016).

In accordance with the thermodynamic estimation, the hornblende crystallized in the hydrous low-pressure environment corresponding

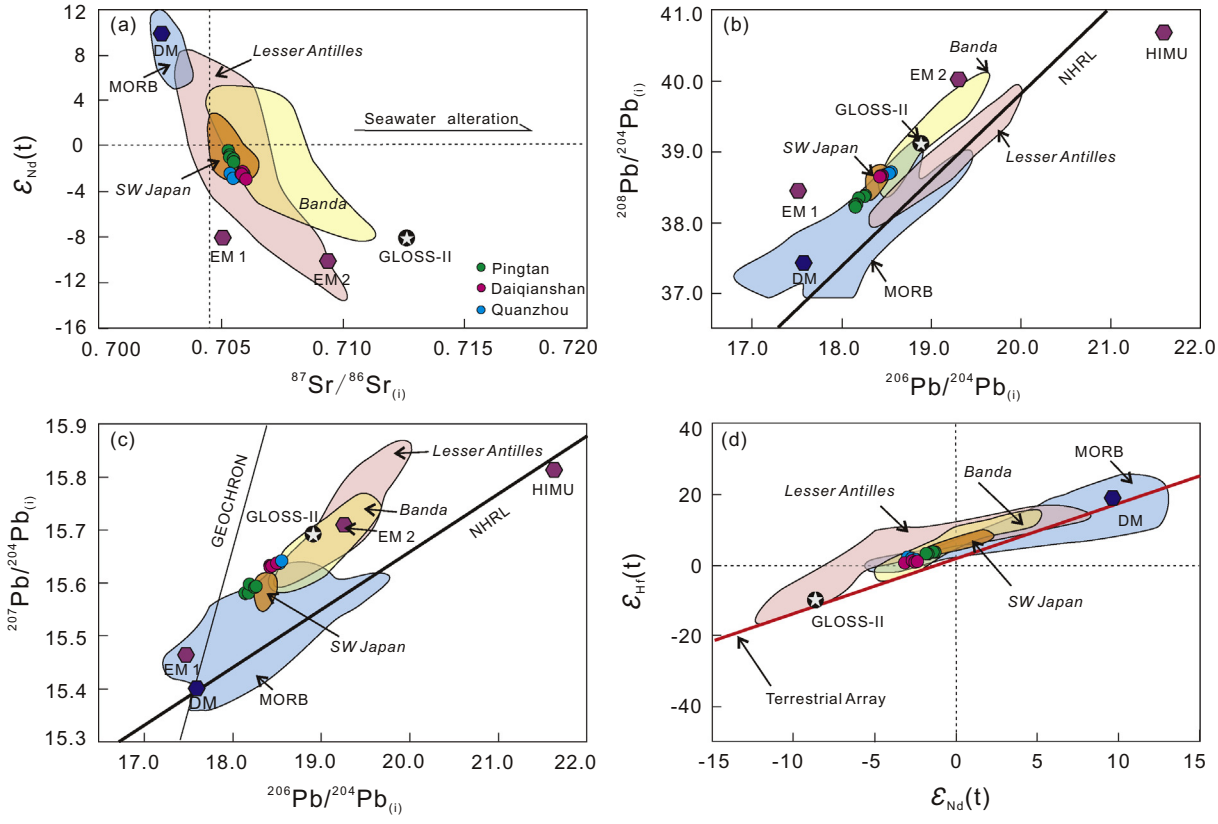

Fig. 9. Diagrams of $^{87}Sr/^{86}Sr_{(i)}$ versus $\varepsilon_{Nd}(t)$ diagram(a), $^{206}Pb/^{204}Pb_{(i)}$ versus $^{208}Pb/^{204}Pb_{(i)}$ (b), $^{206}Pb/^{204}Pb_{(i)}$ versus $^{207}Pb/^{204}Pb_{(i)}$ (c) and $\varepsilon_{Nd}(t)$ versus $\varepsilon_{Hf}(t)$ (d) for the mafic intrusions in SE China. Data sources: DM, EM 1, and EM 2 (Iwamori and Nakamura, 2015; Workman and Hart, 2005); GLOSS-II (Plank, 2014); High-Mg andesites in the SW Japan arc (Ishizaka and Carlson, 1983; Shimoda et al., 1998; Tatsumi et al., 2003); MORB, Calc-alkali volcanic rocks in the Lesser Antilles arc and Banda arc are from Georoc (http://georoc.mpch-mainz.gwdg.de/georoc/); Pingtan (Dong et al., 1997; Li et al., 2018 and this study); Daiqianshan (Wang, 2002 and this study); Quanzhou (Li et al., 2012 and this study).

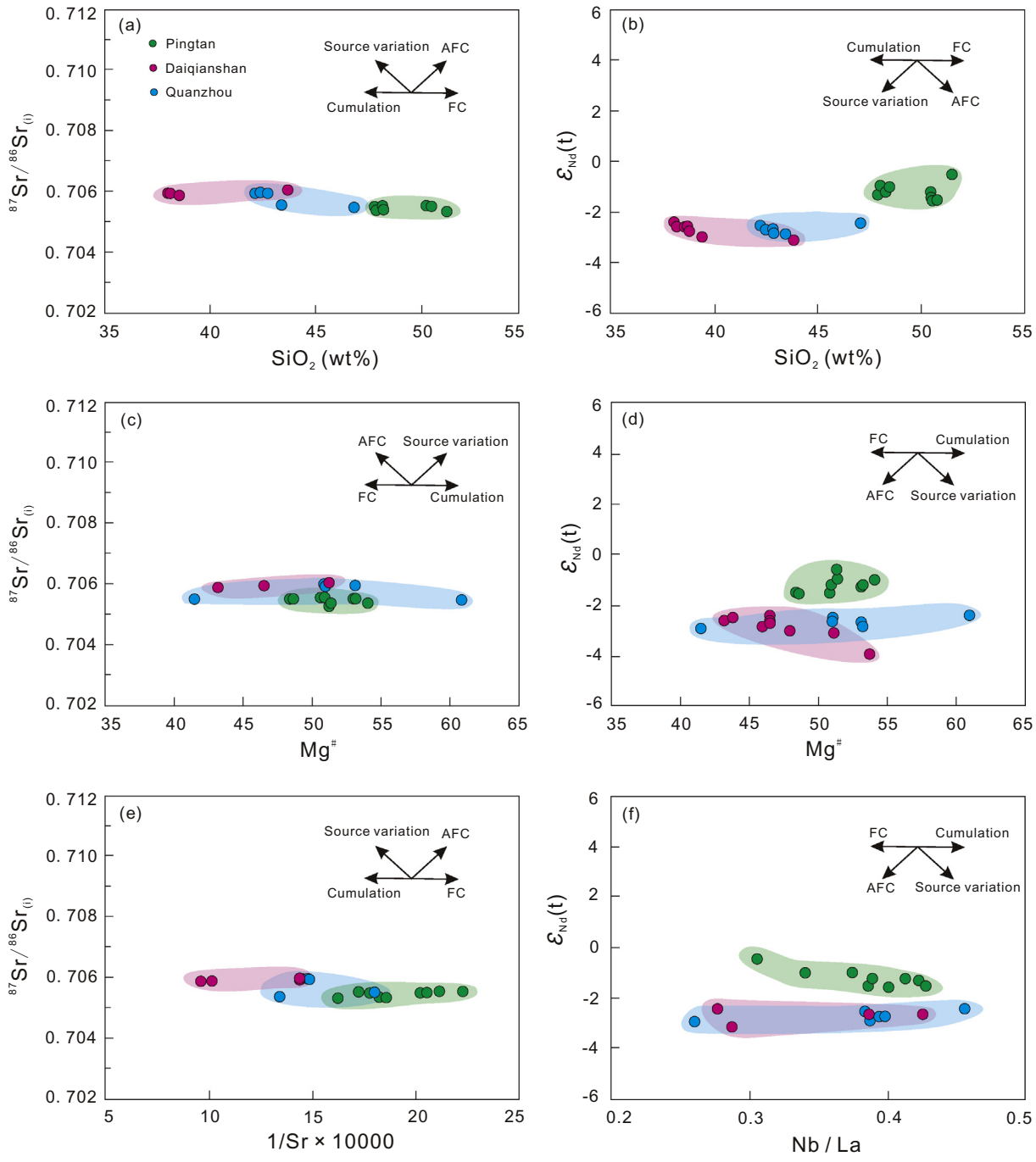

Fig. 10. Diagrams of SiO_2 versus $^{87}Sr/^{86}Sr_{(i)}$ (a), SiO_2 versus $\varepsilon_{Nd}(t)$ (b), $Mg^{\#}$ versus $^{87}Sr/^{86}Sr_{(i)}$ (c), $Mg^{\#}$ versus $\varepsilon_{Nd}(t)$ (d), 1/Sr × 10,000 versus $^{87}Sr/^{86}Sr_{(i)}$ (e) and Nb/La versus $\varepsilon_{Nd}(t)$ (f). Data sources are the same as in Fig. 9.

to the upper crustal levels (103–357 MPa) and at the temperature of 761–924 °C with 4.47–7.57 wt% H_2O. Under such P-T-H_2O conditions, olivine and clinopyroxene may have been crystallized and separated from the residual magmas. This may interpret the rare occurrence of these two mafic phases in the mineral assemblage.

5.2. Estimation of parental magmas

The early Cretaceous mafic intrusions in SE China show variable effects of crystal accumulation, so the whole-rock geochemistry cannot represent the parental magma composition; instead it reflects the sum of composition of the accumulative crystals and trapped melt (Bédard, 1994). Before the using of whole-rock trace element compositions as geochemical indexes, it is necessary to estimate the composition of parental magmas due to hornblende and plagioclase accumulation. Detailed methods and processing procedures were reported by Guo et al. (2016). The parameters for the parental magma calculation are listed in Appended Table S9. The results of the representative sample from each intrusion are illustrated in Fig. 11. With the trapped melt fraction (TMF) ranging between 5% and 20%, the estimated parental magmas in equilibrium with the cumulates show enrichment in LILEs (e.g., Rb, Ba, Th, K) and LREEs but depletions in HFSEs (e.g., Nb, Ta) without positive Sr, Eu and Ti anomalies (Fig. 11). The estimated K_2O contents are ~ 0.8 wt%, 0.7 wt% and 0.5 wt% respectively for the Pingtan, Daiqianshan and Quanzhou intrusions, which are typical for the calc-alkaline arc magmas.

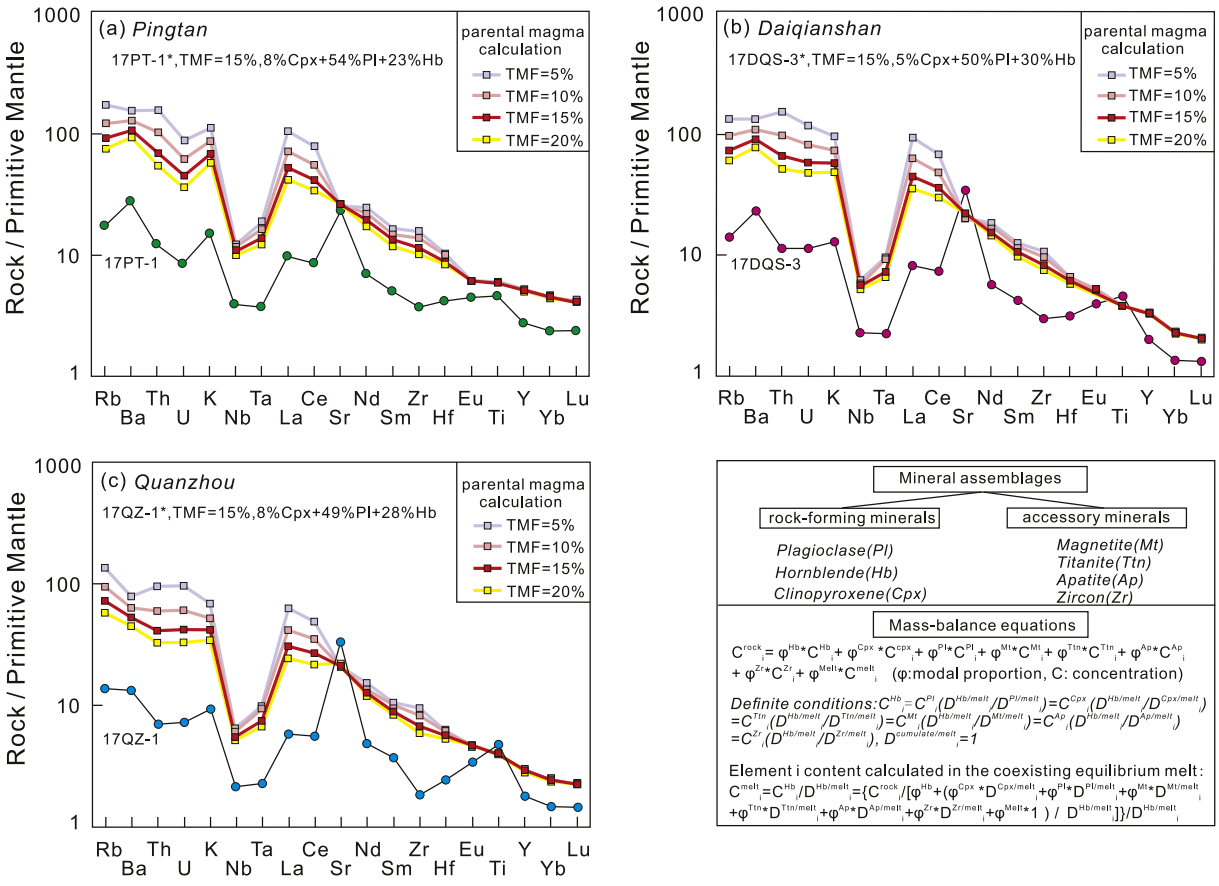

Fig. 11. The estimated compositions of the parental magmas for the mafic intrusions in SE China. Normalized values of primitive mantle are from Sun and McDonough (1989).

Subduction-related calc-alkaline magmas are generally enriched in H_2O (e.g., Grove et al., 2002). Thermodynamic calculation results based on the hornblende compositions yield very high H_2O_{melt} (4.47–7.57 wt%) for the evolved magmas, which are consistent with the presence of hornblende that requires a high H_2O content (> 3 wt %) in the magma system (Smith et al., 2009). However, hornblende is a later crystallizing mineral at low-pressure environment probably corresponding to upper crustal level. In contrast, the plagioclase is an early crystallizing phase as indicated by the petrographic microphotos (Fig. 2). According to Waters and Lange (2015), the plagioclase-liquid hygrometer-thermometer can be applied to melt that span a SiO_2 range of 45–78 wt%. Considering the relatively weak crystal accumulation and moderate SiO_2 content in the Pingtan intrusion, here we adopt the method to estimate the water content of parental magma for crystallization of the calcic plagioclase. The results yield a range of H_2O between 5.6 and 5.9 wt% and confirm a hydrous parental magma for the plagioclase growth. Compared with the Pingtan intrusion, the mafic rocks from the Daiqianshan and Quanzhou intrusions show strong crystal accumulation with SiO_2 <45 wt%, so the plagioclase-liquid hygrometer-thermometer cannot be directly applied to estimate the water contents of parental magma. The plagioclase crystals from these two plutons show relatively narrow compositional ranges and are marked by high calcic component with An numbers as high as 95 and 92, respectively. Calcic plagioclase frequently occurs in subduction-related mafic magmas (e.g., Smith et al., 2009). Previous experimentation suggested that under H_2O-saturated (~6 wt%) condition, a calc-alkaline melt with normal Na_2O and CaO could crystallize anorthite ~ An_{90-95} (Panjasawatwong et al., 1995; Sisson and Grove, 1993). Although calcic plagioclase can also be found in H_2O-undersaturated magmas like MORB, no high-An plagioclase (An >88) has been experimentally produced from natural MORB glass (Kohut and Nielsen, 2003). Therefore, the occurrence of high-An plagioclase from the Daiqianshan and Pingtan intrusions also reflects water-rich parental magmas, consistent with the abundant hornblende in lithology.

In summary, the early Cretaceous mafic intrusions in the coastal region of SE China crystallized from hydrous calc-alkaline parental magmas.

5.3. The role of subducted sediment

5.3.1. The involvement of subducted sediment

The early Cretaceous mafic intrusions in the coastal region of SE China are characterized by high water contents, arc-type trace element geochemistry and “crust-like” isotopic signatures. Since the role of crustal contamination or assimilation is negligible and the fractionation of mafic minerals and plagioclase has little influence on the LILE/HFSE and LREE/HFSE ratios and isotopic compositions, such “crust-like” geochemical features are probably resulted from source enrichment via subduction. In the course of slab subduction, the subducted sediment may transport the crustal signatures into the mantle wedge.

The subducted sediment is the major host for incompatible elements (Plank, 2014), addition even a small amount of sediment will dramatically change the elemental and isotopic compositions of mantle source (Davidson, 1987). The involvement of a subducted sediment component in the studied mafic rocks can be tracked by trace element diagrams such as Th/Sm versus Th/Ce and Th/Yb versus Ba/La (Fig. 12a–b).

The mafic rocks show evolved whole-rock Sr-Nd isotopic compositions and plot along the mixing array between DM and a subducted sediment (Fig. 9), implying the contribution of subducted sediment to the source. Some subduction-related volcanic rocks (e.g., SW Japan, and Lesser Antilles), which also have such “crust-like” Sr and Nd isotope

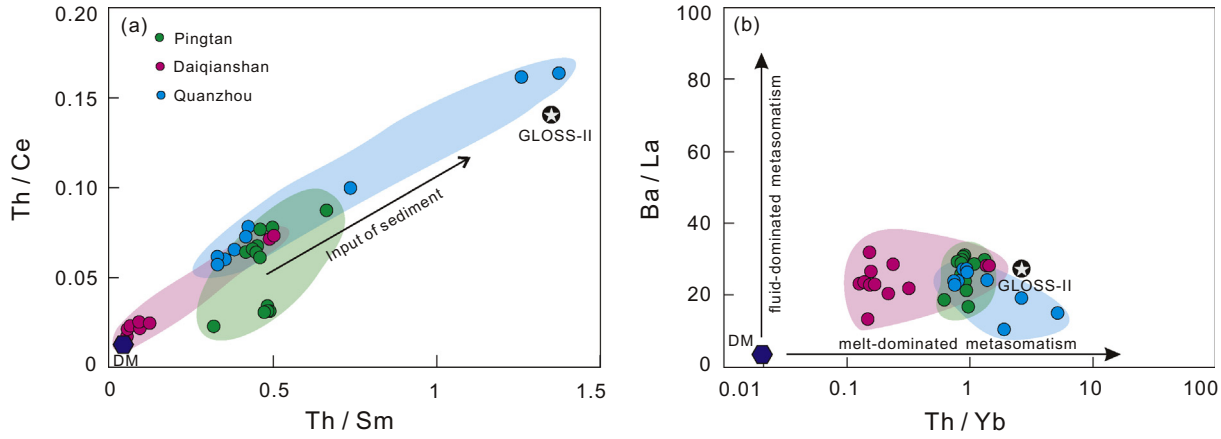

Fig. 12. Diagrams of Th/Sm versus Th/Ce (a) and Th/Yb versus Ba/La (b), showing the involvement of subducted sediment in the depleted mantle. Data sources: GLOSS-II (Plank, 2014); DM (Workman and Hart, 2005); the others are the same as in Fig. 7.

compositions, have been interpreted in terms of variable contribution from the subducted sediment (e.g., Shimoda et al., 1998; White and Dupré, 1986).

Lead isotopes are more sensitive to trace the involvement of subducted sediment in magma source. Addition even a little sediment could rapidly change the Pb isotopic compositions of the samples from the territory of MORB to more radiogenic fields (Kersting and Arculus, 1995). In Fig. 9b and c, the mafic rocks in SE China have highly radiogenic Pb isotopic compositions similar to the high-Mg andesites in SW Japan and plot above the Northern Hemisphere Reference Line (NHRL). Both the plagioclase crystals and the whole-rock samples constitute a mixing trend between DM and a subducted sediment component (Figs. 6b and 9b–c). The Pb isotopic variations among the three intrusions can be interpreted by different proportional mixing between the DM and subducted sediment.

Apart from the Sr-Nd-Pb isotopes, the relationship between Hf and Nd isotopes can also provide useful information to constrain the contribution of a subducted component (Chauvel et al., 2008). Hafnium and Nd isotopes of the mafic intrusions plot above the terrestrial array (Fig. 9d), and also fall within the variation field between MORB and the subducted sediment. Such a Hf-Nd isotopic decoupling phenomenon (elevated $\varepsilon_{Hf}(t)$ at a given $\varepsilon_{Nd}(t)$) in our samples is widely observed in modern arc magmas like those in SW Japan, Lesser Antilles and Banda, in which subducted sediment have been involved in the magmatic origin (Hanyu et al., 2002; Labanieh et al., 2010; Nebel et al., 2011).

Collectively, the elemental and Sr-Nd-Pb-Hf isotopic features of the early Cretaceous mafic intrusions in SE China indicate the contribution of subducted sediment to the mantle wedge in response to subduction of the Paleo-Pacific Ocean.

5.3.2. Fluid via melt metasomatism?

In subduction zones, slab-derived fluid and melt are regarded as the most important agents to interpret the LILE and LREE enrichment and HFSE depletion in arc magmas. Previous studies have demonstrated that a combination of whole-rock Hf and Nd isotope data with some incompatible trace element ratios (e.g., Ba/Nb and Ba/La) that are insensitive to crystal accumulation, is feasible to investigate the metasomatic agent and to estimate the proportion of subducted sediment (Guo et al., 2015; Hanyu et al., 2002). Thus, we use such quantitative methods to estimate the proportion of the subducted sediment that had been input into the magma sources, and the melting degrees to generate the parental magmas of the mafic intrusions.

We select the average geochemical compositions reported by Plank (2014) to represent the sediment end-member component. The other end-member component is a depleted mantle estimated by Sun and McDonough (1989). Detailed calculation parameters are shown in Fig. 13. The modeling results suggest that a variable proportion (3–5%) of melt derived from the subducted sediment was involved into the mantle sources for the mafic intrusions in SE China. The Th-rich geochemical nature of the estimated parental magmas also favors the contribution of sediment melts (Fig. 11), since Th is immobile by aqueous fluids but it can be transferred from the subducted slab to the mantle wedge, in the case that sediment-derived melt acts as the predominant metasomatic agent (Johnson and Plank, 1999).

The modeling results also suggest that 5–20% melting of a sediment melt-metasomatized mantle wedge could generate the trace element concentrations of calculated parental magma of the Pingtan intrusion (Fig. 14a). Similar degrees of melting of the metasomatized mantle can also produce the parental magmas for the Daiqianshan and Quanzhou mafic intrusions (Fig. 14b and c). Our element-isotopic modeling results demonstrate the importance of subducted sediment-derived melt in the mantle enrichment beneath the coastal region of SE China during early Cretaceous.

5.4. Implications for subduction of the Paleo-Pacific Ocean

Subduction of the Paleo-Pacific Ocean has widely been accepted to interpret the Mesozoic tectono-magmatic activities in SE China (e.g., Li et al., 2014; Wang et al., 2011; Zhou et al., 2006), although debate remains about the petrogenesis of late Mesozoic igneous rocks (e.g., Li, 2000; Zhou and Li, 2000). Previous studies even suggested that the influence of Paleo-Pacific Ocean subduction in SE China could be tracked back as early as to ~ 180 Ma (e.g., Zhou and Li, 2000). Nevertheless, the robust petrologic and geochemical evidence for late Mesozoic subduction of the Paleo-Pacific Ocean in SE China is still lacking. One explanation is that the geological records of Mesozoic subduction of the Paleo-Pacific Ocean had been destructed by late Mesozoic-early Cenozoic tectonic superposition (Mao et al., 2014). Another interpretation is attributed to the strike-slipping movement of terranes induced by the NE-trending sinistral strike-slip faults (Gilder et al., 1996), e.g., the Cretaceous SW Japan accretionary prism had been initially located in the continental margin of the Cathaysia Block and was northward drifted to its present situation (e.g., Maruyama et al., 1997). In contrast with these two hypotheses, our results from the early Cretaceous mafic intrusions in SE China provide critical petrogenetic and geochemical constraints on subduction of the Paleo-Pacific Ocean. In the course of slab subduction, silicate melt derived from the subducted sediment reacted with the mantle wedge to form the metasomatized mantle source (Fig. 15). Partial melting of the metasomatized mantle wedge produced the parental magmas, which experienced fractionation of ferromagnesian minerals (e.g., olivine and clinopyroxene) at great depths

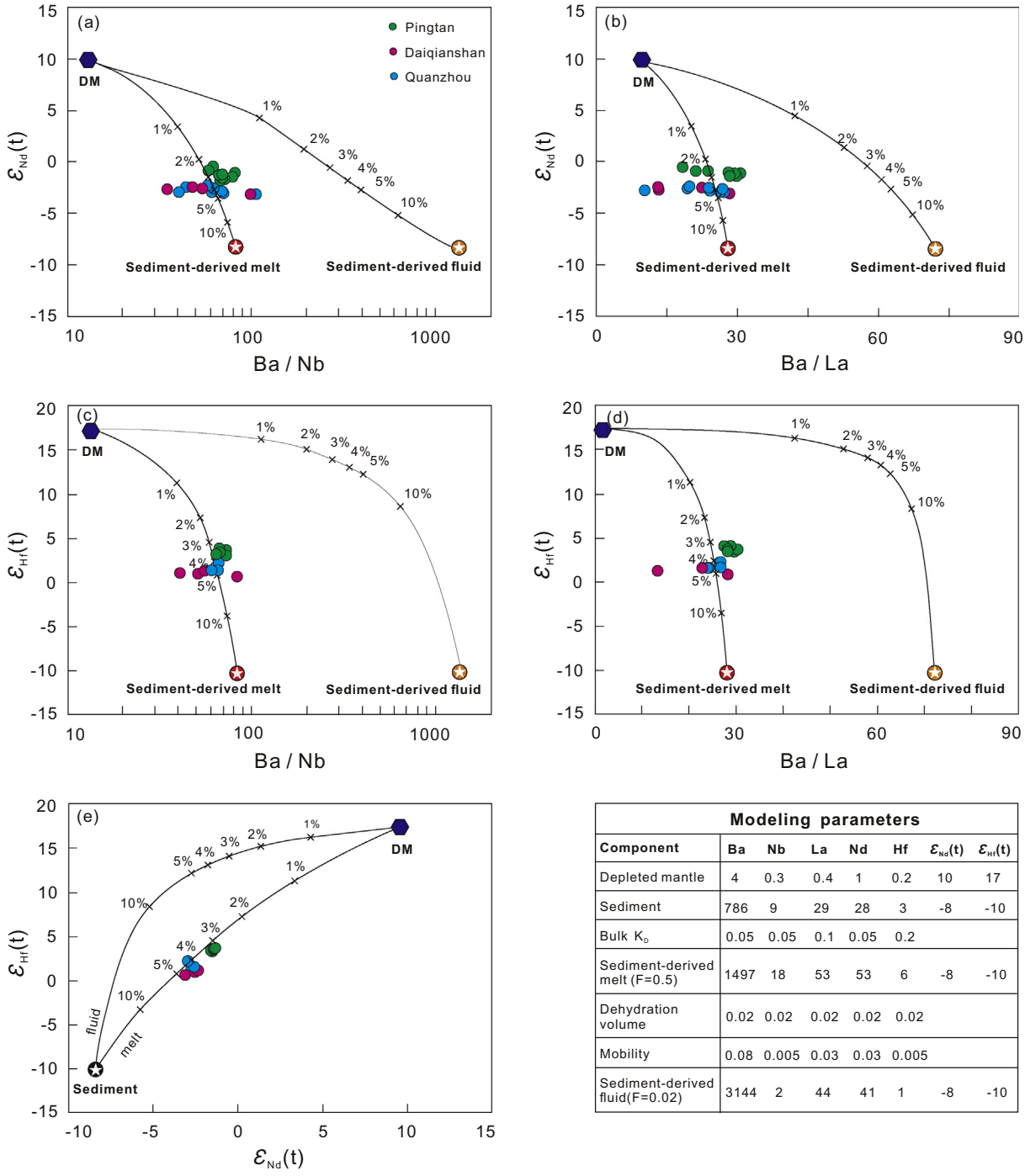

Modeling parameters

Component	Ba	Nb	La	Nd	Hf	$\varepsilon_{Nd}(t)$	$\varepsilon_{Hf}(t)$
Depleted mantle	4	0.3	0.4	1	0.2	10	17
Sediment	786	9	29	28	3	-8	-10
Bulk K_D	0.05	0.05	0.1	0.05	0.2		
Sediment-derived melt (F=0.5)	1497	18	53	53	6	-8	-10
Dehydration volume	0.02	0.02	0.02	0.02	0.02		
Mobility	0.08	0.005	0.03	0.03	0.005		
Sediment-derived fluid(F=0.02)	3144	2	44	41	1	-8	-10

Fig. 13. Diagrams of Ba/Nb versus $\varepsilon_{Nd}(t)$ (a), Ba/La versus $\varepsilon_{Nd}(t)$ (b), Ba/Nb versus $\varepsilon_{Hf}(t)$ (c), Ba/La versus $\varepsilon_{Hf}(t)$ (d) and $\varepsilon_{Nd}(t)$ versus $\varepsilon_{Hf}(t)$ (e) of early Cretaceous mafic intrusions (after Guo et al., 2015). The Ba, Nb, La, Nd and Hf concentrations of DM are assumed to be low than those of primitive mantle. The compositions of the subducted sediment (GLOSS-II) are from Plank (2014). $\varepsilon_{Nd}(t)$ and $\varepsilon_{Hf}(t)$ of DM are calculated using the average values for MORB (Workman and Hart, 2005), whereas $\varepsilon_{Nd}(t)$ and $\varepsilon_{Hf}(t)$ of GLOSS-II are estimated to be −8 and − 10, respectively (Plank, 2014). The bulk partition coefficients (K_D) during sediment melting, the elemental mobility in aqueous fluid and the dehydration volume released from sediment are followed from Guo et al. (2016) and Alzawa et al. (1999).

and were then emplaced into the upper crustal magma chambers to accumulate plagioclase and hornblende (Fig. 15).

The early Cretaceous mafic intrusions in the coastal region of SE China generally show "crust-like" isotopic signatures similar to those subduction-related volcanic rocks from the SW Japan, Lesser Antilles and Banda arcs. A common feature of these modern subduction zones is the predominance of sediment melting in the course of slab subduction, which requires a relatively hot geotherm (e.g., Furukawa and Tatsumi, 1999; Watt et al., 2013). Such a hot thermal structure beneath modern subduction zone is mainly affected by the thermal state of subducted oceanic lithosphere, which is relevant to the age and/or surface temperature of the oceanic slab (Iwamori et al., 2007). Results from plate reconstruction are consistent with the young and hot subducting oceanic lithosphere beneath the SW Japan, Lesser Antilles and Banda arcs (Seton et al., 2012). Thus, hydrous melting of the subducted sediment is feasible as hydrous minerals can release water at relatively shallow depths in such relatively hot subduction zones (Plank et al., 2009). Similarly, plate reconstruction also indicated that the subducted early

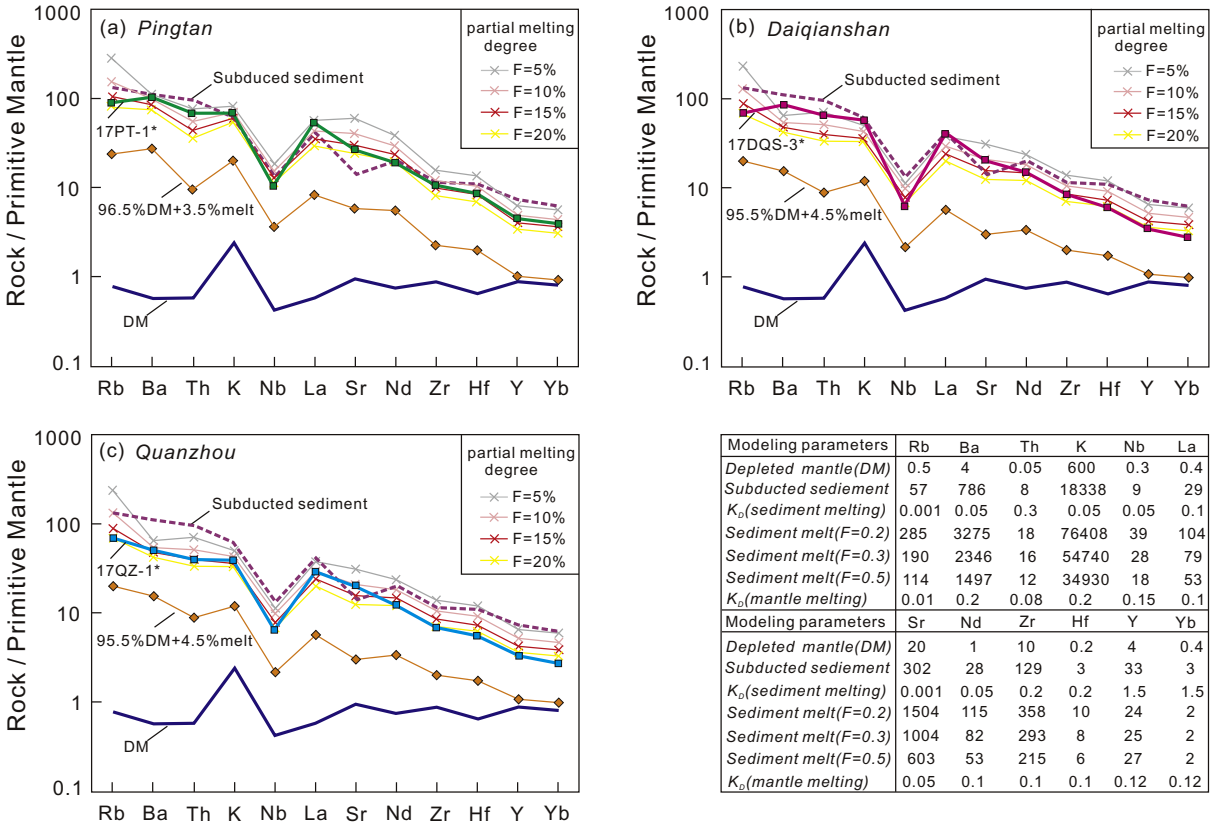

Modeling parameters	Rb	Ba	Th	K	Nb	La
Depleted mantle(DM)	0.5	4	0.05	600	0.3	0.4
Subducted sediement	57	786	8	18338	9	29
K_D(sediment melting)	0.001	0.05	0.3	0.05	0.05	0.1
Sediment melt(F=0.2)	285	3275	18	76408	39	104
Sediment melt(F=0.3)	190	2346	16	54740	28	79
Sediment melt(F=0.5)	114	1497	12	34930	18	53
K_D(mantle melting)	0.01	0.2	0.08	0.2	0.15	0.1
Modeling parameters	Sr	Nd	Zr	Hf	Y	Yb
Depleted mantle(DM)	20	1	10	0.2	4	0.4
Subducted sediement	302	28	129	3	33	3
K_D(sediment melting)	0.001	0.05	0.2	0.2	1.5	1.5
Sediment melt(F=0.2)	1504	115	358	10	24	2
Sediment melt(F=0.3)	1004	82	293	8	25	2
Sediment melt(F=0.5)	603	53	215	6	27	2
K_D(mantle melting)	0.05	0.1	0.1	0.1	0.12	0.12

Fig. 14. PM-normalized spidergrams of incompatible trace element modeling results of the early Cretaceous mafic intrusions in SE China. Normalized values of primitive mantle are from Sun and McDonough (1989).

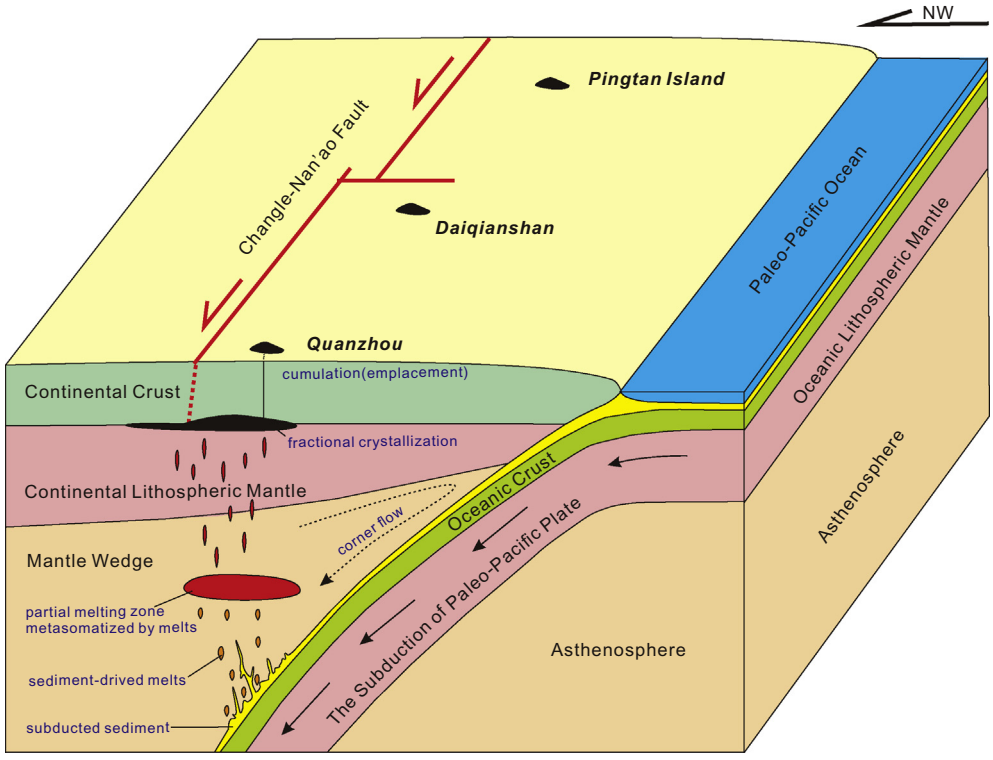

Fig. 15. A schematic diagram showing the formation of the early Cretaceous mafic intrusions in SE China in response to subduction of the Paleo-Pacific Ocean.

Cretaceous Paleo-Pacific slab was relatively young and hot beneath the coastal region of SE China (e.g., Seton et al., 2012) and could provide enough heat to melt the subducted sediment. It is therefore likely that melting of the subducted sediment may be an important way to mantle enrichment beneath the relatively hot subduction zones.

6. Conclusions

Our comprehensive data from geochronology, petrology and geochemistry indicate that the early Cretaceous mafic intrusions from the coastal region of SE China were formed in response to subduction of the Paleo-Pacific Ocean, during which the subducted sediment-derived melt was the predominant agent to enrich the mantle wedge. The following conclusions can be summarized:

(1) The new zircon U-Pb dating results by SIMS indicate an extensive mafic magmatism during early Cretaceous with a narrow age range from 116 to 113 Ma.
(2) The parental magmas of the early Cretaceous mafic intrusions are hydrous and calc-alkaline, characterized by arc-type trace element geochemistry with "crust-like" isotopic signatures.
(3) The mafic intrusions were initially formed via 5–20% melting of a depleted mantle source metasomatized by addition of 3–5% subducted sediment-derived melt. The parental magmas then experienced fractionation of mafic minerals and accumulation of plagioclase and hornblende in crustal magma chambers.
(4) Extensive melting of the subducted sediment suggests a relatively hot subduction zone beneath the coastal region of SE China, as observed in modern subduction zones such as the SW Japan, Lesser Antilles and Banda arcs.

Supplementary data to this article can be found online at https://doi.org/10.1016/j.lithos.2019.03.010.

Acknowledgements

We appreciate Mr. Zhang Le to help in-situ Sr-Pb analyses on plagioclase and Ms. Chen Linli for electronic microprobe analyses, Dr. Tu Xianglin for ICP-MS analyses, Prof. Li Qiuli for SIMS analyses, and Prof. Zhang Zhaofeng for Sr-Nd-Pb-Hf isotope analyses. Constructive comments from Dr. Li Zhen, an anomynous referee and the Editor help to improve the paper. This study was financially supported by the National Science Foundation of China (Grant Nos. 41525006 and U1701641), the Strategic Priority Research Program (B) of Chinese Academy of Sciences (Grant XDB 18000000), and the Department of Science and Technology of Guangdong Province (2015TX01Z219). This is contribution No.IS-2669 from GIGCAS.

References

Alzawa, Y., Tatsumi, Y., Yamada, H., 1999. Element transport by dehydration of subducted sediments: Implication for arc and ocean island magmatism. Island Arc 8, 38–46. https://doi.org/10.1046/j.1440-1738.1999.00217.x.

Barry, T.L., Pearce, J.A., Leat, P.T., Millar, I.L., Roex le, A.P., 2006. Hf isotope evidence for selective mobility of high-field-strength elements in a subduction setting: South Sandwich Islands. Earth and Planetary Science Letters 252, 223–244. https://doi.org/10.1016/j.epsl.2006.09.034.

Bédard, J.H., 1994. A procedure for calculating the equilibrium distribution of trace elements among the minerals of cumulate rocks, and the concentration of trace elements in the coexisting liquids. Chemical Geology 118, 143–153. https://doi.org/10.1016/0009-2541(94)90173-2.

Bezard, R., Turner, S., Davidson, J.P., Macpherson, C.G., Lindsay, J.M., 2015. Seeing through the effects of crustal assimilation to assess the source composition beneath the Southern Lesser Antilles arc. Journal of Petrology 0, 1–30. https://doi.org/10.1093/petrology/egv018.

Chauvel, C., Lewin, E., Carpentier, M., Arndt, N.T., Marini, J.C., 2008. Role of recycled oceanic basalt and sediment in generating the Hf-Nd mantle array. Nature Geoscience 1, 64–67. https://doi.org/10.1038/ngeo.2007.51.

Chen, W.S., Yang, H.C., Wang, X., Huang, H., 2002. Tectonic setting and exhumation history of the Pingtan-Dongshan metamorphic belt along the coastal area, Fujian Province, Southeast. Journal of Asian Earth Sciences 20, 829–840. https://doi.org/10.1016/S1367-9120(01)00066-9.

Chen, C.H., Lin, W., Lan, C.Y., Lee, C.Y., 2007. Geochemical, Sr and Nd isotopic characteristics and tectonic implications for three stages of igneous rock in the late Yanshanian (cretaceous) orogeny, SE China. Transactions of the Royal Society of Edinburgh: Earth Sciences 95, 237–248. https://doi.org/10.1017/S0263593300001048.

Chiaradia, M., Müntener, O., Beate, B., 2011. Enriched basaltic andesites from mid-crustal fractional crystallization, recharge, and assimilation (Pilavo volcano, Western Cordillera of Ecuador). Journal of Petrology 52, 1107–1141. https://doi.org/10.1093/petrology/egr020.

Clift, P.D., Rose, E.F., Shimizu, N., Layne, G.D., Draut, A.E., Regelous, M., 2001. Tracing the evolving flux from the subducting plate in the Tonga-Kermadec arc system using boron in volcanic glass. Geochimica et Cosmochimica Acta 65, 3347–3364. https://doi.org/10.1016/S0016-7037(01)00670-6.

Davidson, J.P., 1987. Crustal contamination versus subduction zone enrichment: examples from the Lesser Antilles and implications for mantle source compositions of island arc volcanic rocks. Geochemica et Cosmochimica Acta 51, 2185–2198. https://doi.org/10.1016/0016-7037(87)90268-7.

Dong, C.W., Zhou, X.M., Li, H.M., Ren, S.L., Zhou, X.H., 1997. Late Mesozoic crust mantle interaction in Southeastern Fujian: Isotopic evidence from Pingtan igneous complex. Chinese Science Bulletin 42, 495–498. https://doi.org/10.1007/BF02882602.

Elburg, M., Vroon, P., van der Wagt, B., Tchalikian, A., 2005. Sr and Pb isotopic composition of five USGS glasses (BHVO-2G, BIR-1G, BCR-2G, TB-1G, NKT-1G). Chemical Geology 223, 196–207. https://doi.org/10.1016/j.chemgeo.2005.07.001.

Furukawa, Y., Tatsumi, Y., 1999. Melting of a subducting slab and production of high-Mg andesite magmas: Unusual magmatism in SW Japan at 13-15 Ma. Geophysical Research Letters 26, 2271–2274. https://doi.org/10.1029/1999GL900512.

Gilder, S.A., Gill, J., Coe, R.S., Zhao, X.X., Liu, Z.W., Wang, G.X., Yuan, K.R., Liu, W.L., Kuang, G.D., Wu, H.R., 1996. Isotopic and paleomagnetic constraints on the Mesozoic tectonic evolution of South China. Journal of Geophysical Research 101, 16137–16154. https://doi.org/10.1029/96JB00662.

Grove, T., Parman, S., Bowring, S., Price, R., Baker, M., 2002. The role of an H_2O-rich fluid component in the generation of primitive basaltic andesites and andesites from the Mt. Shasta region, N California. Contributions to Mineralogy and Petrology 142, 375–396. https://doi.org/10.1007/s004100100299.

Guo, F., Li, H.X., Fan, W.M., Li, J.Y., Zhao, L., Huang, M.W., Xu, W.L., 2015. Early Jurassic subduction of the Paleo-Pacific Ocean in NE China: Petrologic and geochemical evidence from the Tumen mafic intrusive complex. Lithos 224–225, 46–60. https://doi.org/10.1016/j.lithos.2015.02.014.

Guo, F., Li, H.X., Fan, W.M., Li, J.Y., Zhao, L., Huang, M.W., 2016. Variable sediment flux in generation of Permian subduction-related mafic intrusions from the Yanbian region, NE China. Lithos 261, 195–215. https://doi.org/10.1016/j.lithos.2015.11.030.

Hanyu, T., Tatsumi, Y., Nakai, S., 2002. A contribution of slab-melts to the formation of high-Mg andesite magmas; Hf isotopic evidence from SW Japan. Geophysical Research Letters 29, 8–1-8–4. https://doi.org/10.1029/2002GL015856.

Hauff, F., Hoernle, K., Schmidt, A., 2003. Sr-Nd-Pb composition of Mesozoic Pacific oceanic crust (Site 1149 and 801, ODP Leg 185): Implications for alteration of ocean crust and the input into the Izu-Bonin-Mariana subduction system. Geochemistry, Geophysics, Geosystems 4. https://doi.org/10.1029/2002GC000421.

Hawthorne, F.C., Oberti, R., 2006. On the classification of amphiboles. Canadian Mineralogist 44, 1–21. https://doi.org/10.2113/gscanmin.44.1.1.

Hermann, J., Spandler, C.J., 2008. Sediment melts at sub-arc depths: an experimental study. Journal of Petrology 49, 717–740. https://doi.org/10.1093/petrology/egm073.

Humphreys, M.C.S., Blundy, J.D., Sparks, R.S.J., 2006. Magma evolution and open-system processes at Shiveluch volcano: Insights from phenocryst zoning. Journal of Petrology 47, 2303–2334. https://doi.org/10.1093/petrology/egl045.

Ishizaka, K., Carlson, R.W., 1983. Nd-Sr systematics of the Setouchi volcanic rocks, Southwest Japan: a clue to the origin of orogenic andesite. Earth and Planetary Science Letters 64, 327–340. https://doi.org/10.1016/0012-821X(83)90094-8.

Iwamori, H., Nakamura, H., 2015. Isotopic heterogeneity of oceanic, arc and continental basalts and its implications for mantle dynamics. Gondwana Research 27, 1131–1152. https://doi.org/10.1016/j.gr.2014.09.003.

Iwamori, H., Richardson, C., Maruyama, S., 2007. Numerical modeling of thermal structure, circulation of H_2O, and magmatism-metamorphism in subduction zones: Implications for evolution of arcs. Gondwana Research 11, 109–119. https://doi.org/10.1016/j.gr.2006.04.010.

Johnson, M.C., Plank, T., 1999. Dehydration and melting experiments constrain the fate of subducted sediments. Geochemistry, Geophysics, Geosystems 1, 1007. https://doi.org/10.1029/1999GC000014.

Kersting, A.B., Arculus, R.J., 1995. Pb systematics of Klyuchevskoy volcano, Kamchatka, and North Pacific sediments: Implications for magma genesis and sediment recycling in the Kamchatkan arc. Earth and Planetary Science Letters 136, 133–148. https://doi.org/10.1180/minmag.1994.58A.1.246.

Kohut, E.J., Nielsen, R.L., 2003. Low-pressure phase equilibria of anhydrous anorthite-bearing mafic magmas. Geochemistry, Geophysics, Geosystems 4, 1057. https://doi.org/10.1029/2002GC000451.

Labanieh, S., Chauvel, C., Germa, A., Quidelleur, X., Lewin, E., 2010. Isotopic hyperbolas constrain sources and processes under the Lesser Antilles arc. Earth and Planetary Science Letters 298, 35–46. https://doi.org/10.1016/j.epsl.2010.07.018.

Li, X.H., 2000. Cretaceous magmatism and lithospheric extension in Southeast China. Journal of Asian Earth Sciences 18, 293–305. https://doi.org/10.1016/S1367-9120(99)00060-7.

Li, H.M., Dong, C.W., Xu, X.S., Zhou, X.M., 1995. Single-zircon U-Pb dating for Quanzhou gabbro: the origin of the basic magmatic rocks. Chinese Science Bulletin 40, 158 (in Chinese with English abstract).

Li, X.H., Qi, C.S., Liu, Y., Liang, X.R., Tu, X.L., L., W., W., X., Yang, Y.H., 2005. Rapid separation of Hf from rock samples for isotope analysis by MC-ICPMS: a modified single-column

extraction chromatography method. Geochimica 109–114, 34 (in Chinese with English abstract).
Li, X.H., Li, Z.X., Wingate, M.T.D., Chung, S.L., Liu, Y., Lin, G.C., Li, W.X., 2006. Geochemistry of the 755 Ma Mundine well dyke swarm, northwestern Australia: part of a Neoproterozoic mantle superplume beneath Rodinia? Precambrian Research 146, 1–15. https://doi.org/10.1016/j.precamres.2005.12.007.
Li, X.H., Liu, Y., Li, Q.L., Guo, C.H., Chamberlain, K.R., 2009. Precise determination of Phanerozoic zircon Pb/Pb age by multicollector SIMS without external standardization. Geochemistry, Geophysics, Geosystems 10, 1–21. https://doi.org/10.1029/2009GC002400.
Li, Z., Qiu, J.S., Xu, X.S., 2012. Geochronological, geochemical and Sr-Nd-Hf isotopic constraints on petrogenesis of late Mesozoic gabbro-granite complexes on the Southeast coast of Fujian, South China: Insights into a depleted mantle source region and crust-mantle interactions. Geological Magazine 149, 459–482. https://doi.org/10.1017/S0016756811000793.
Li, X.H., Tang, G.Q., Gong, B., Yang, Y.H., Hou, K.J., Hu, Z.C., Li, Q.L., Liu, Y., Li, W.X., 2013. Qinghu zircon: a working reference for microbeam analysis of U-Pb age and Hf and O isotopes. Chinese Science Bulletin 58, 4647–4654. https://doi.org/10.1007/s11434-013-5932-x.
Li, Z., Qiu, J.S., Yang, X.M., 2014. A review of the geochronology and geochemistry of late Yanshanian (cretaceous) plutons along the Fujian coastal area of Southeastern China: Implications for magma evolution related to slab break-off and rollback in the cretaceous. Earth-Science Reviews 128, 232–248. https://doi.org/10.1016/j.earscirev.2013.09.007.
Li, Z., Wang, X.C., Wilde, S.A., Liu, L., Li, W.X., Yang, X., 2018. Role of deep-Earth water cycling in the growth and evolution of continental crust: constraints from cretaceous magmatism in Southeast China. Lithos 302–303, 126–141. https://doi.org/10.1016/j.lithos.2017.12.028.
Liu, Y., Liu, H.C., Li, X.H., 1996. Simultaneous and precise determination of 40 trace element elements using ICP-MS. Geochimica 25, 552–558 (in Chinese with English abstract).
Ludwig, K.R., 2003. User's manual for Isoplot 3.00: a geochronological toolkit for Microsoft Excel. Berkeley Geochronology Center Special Publication 4, 71. https://doi.org/10.1002/eqe.3063.
Mallik, A., Dasgupta, R., Tsuno, K., Nelson, J., 2016. Effects of water, depth and temperature on partial melting of mantle-wedge fluxed by hydrous sediment-melt in subduction zones. Geochimica et Cosmochimica Acta 195, 226–243. https://doi.org/10.1016/j.gca.2016.08.018.
Mao, J.R., Li, Z.L., Ye, H.M., 2014. Mesozoic tectono-magmatic activities in South China: Retrospect and prospect. Science China Earth Sciences 57, 2853–2877. https://doi.org/10.1007/s11430-014-5006-1.
Maruyama, S., Isozaki, Y., Kimura, G., Terabayashi, M., 1997. Paleogeographic maps of the Japanese islands: Plate tectonic synthesis from 750 Ma to the present. Island Arc 6, 121–142. https://doi.org/10.1111/j.1440-1738.1997.tb00043.x.
Mazzeo, F.C., D'Antonio, M., Arienzo, I., Aulinas, M., Di Renzo, V., Gimeno, D., 2014. Subduction-related enrichment of the Neapolitan volcanoes (Southern Italy) mantle source: New constraints on the characteristics of the slab-derived components. Chemical Geology 386, 165–183. https://doi.org/10.1016/j.chemgeo.2014.08.014.
Nebel, O., Vroon, P.Z., Westrenen, W.van., Iizuka, T., Davies, G.R., 2011. The effect of sediment recycling in subduction zones on the Hf isotope character of new arc crust, Banda arc, Indonesia. Earth and Planetary Science Letters 303, 240–250. https://doi.org/10.1016/j.epsl.2010.12.053.
Nelson, S.T., Montana, A., 1992. Sieve-textured plagioclase in volcanic rocks produced by rapid decompression. American Mineralogist 77, 1242–1249. https://doi.org/10.1180/minmag.1992.056.385.19.
Nichols, G.T., Wyllie, P.J., Stern, C.R., 1994. Subduction zone melting of pelagic sediments constrained by melting experiments. Nature 371, 785–788. https://doi.org/10.1038/371785a0.
Panjasawatwong, Y., Danyushevsky, L.V., Crawford, A.J., Harris, K.L., 1995. An experimental study of the effects of melt composition on plagioclase-melt equilibria at 5 and 10 kbar: Implications for the origin of magmatic high-an plagioclase. Contributions to Mineralogy and Petrology 118, 420–432. https://doi.org/10.1007/s004100050024.
Parsons, I., 2010. Feldspars defined and described: a pair of posters published by the Mineralogical Society. Sources and supporting information. Mineralogical Magazine 74, 529–551. https://doi.org/10.1180/minmag.2010.074.3.529.
Plank, T., 2014. The chemical composition of subducting sediments. Treatise on Geochemistry: Second Edition, 2nd ed Elsevier Ltd. https://doi.org/10.1016/B978-0-08-095975-7.00319-3.
Plank, T., Langmuir, C.H., 1998. The chemical composition of subducting sediment and its consequences for the crust and mantle. Chemical Geology 145, 325–394. https://doi.org/10.1016/S0009-2541(97)00150-2.
Plank, T., Cooper, L.B., Manning, C.E., 2009. Emerging geothermometers for estimating slab surface temperatures. Nature Geoscience 2, 611–615. https://doi.org/10.1038/ngeo614.
Ribeiro, J.M., Stern, R.J., Kelley, K.A., Martinez, F., Ishizuka, O., Manton, W.I., Ohara, Y., 2013. Nature and distribution of slab-derived fluids and mantle sources beneath the Southeast Mariana forearc rift. Geochemistry, Geophysics, Geosystems 14, 4585–4607. https://doi.org/10.1002/ggge.20244.
Ridolfi, F., Renzulli, A., 2012. Calcic amphiboles in calc-alkaline and alkaline magmas: Thermobarometric and chemometric empirical equations valid up to 1,130 °C and 2.2 GPa. Contributions to Mineralogy and Petrology 163, 877–895. https://doi.org/10.1007/s00410-011-0704-6.
Seton, M., Müller, R.D., Zahirovic, S., Gaina, C., Torsvik, T., Shephard, G., Talsma, A., Gurnis, M., Turner, M., Maus, S., Chandler, M., 2012. Global continental and ocean basin reconstructions since 200Ma. Earth-Science Reviews 113, 212–270. https://doi.org/10.1016/j.earscirev.2012.03.002.
Shimoda, G., Tatsumi, Y., Nohda, S., Ishizaka, K., Jahn, B.M., 1998. Setouchi high-Mg andesites revisited: Geochemical evidence for melting of subducting sediments. Earth and Planetary Science Letters 160, 479–492. https://doi.org/10.1016/S0012-821X(98)00105-8.
Sisson, T.W., Grove, T.L., 1993. Experimental investigations of the role of H_2O in calc-alkaline differentiation and subduction zone magmatism. Contributions to Mineralogy and Petrology 113, 143–166. https://doi.org/10.1007/BF00283225.
Sláma, J., Košler, J., Condon, D.J., Crowley, J.L., Gerdes, A., Hanchar, J.M., Horstwood, M.S.A., Morris, G.A., Nasdala, L., Norberg, N., Schaltegger, U., Schoene, B., Tubrett, M.N., Whitehouse, M.J., 2008. Plešovice zircon - a new natural reference material for U-Pb and Hf isotopic microanalysis. Chemical Geology 249, 1–35. https://doi.org/10.1016/j.chemgeo.2007.11.005.
Smith, D.J., Petterson, M.G., Saunders, A.D., Millar, I.L., Jenkin, G.R.T., Toba, T., Naden, J., Cook, J.M., 2009. The petrogenesis of sodic island arc magmas at Savo volcano, Solomon islands. Contributions to Mineralogy and Petrology 158, 785–801. https://doi.org/10.1007/s00410-009-0410-9.
Sun, S.S., McDonough, W.F., 1989. Chemical and isotopic systematics of oceanic basalts: Implications for mantle composition and processes. Geological Society, London, Special Publications 42, 313–345. https://doi.org/10.1144/GSL.SP.1989.042.01.19.
Tamura, Y., Tani, K., Chang, Q., Shukuno, H., Kawabata, H., Ishizuka, O., Fiske, R.S., 2007. Wet and dry basalt magma evolution at Torishima volcano, Izu-Bonin arc, Japan: the possible role of phengite in the downgoing slab. Journal of Petrology 48, 1999–2031. https://doi.org/10.1093/petrology/egm048.
Tatsumi, Y., Shukuno, H., Sato, K., Shibata, T., Yoshikawa, M., 2003. The petrology and geochemistry of high-magnesium andesites at the Western tip of the Setouchi volcanic belt, SW Japan. Journal of Petrology 44, 1561–1578. https://doi.org/10.1093/petrology/egg049.
Todt, W., Cliff, R.A., Hanser, A., Hofmann, A.W., 1996. Evaluation of a $^{202}Pb-^{205}Pb$ double spike for high-precision lead isotope analysis. Geophysical Monograph Series 95, 429–437. https://doi.org/10.1029/GM095p0429.
Vroon, P.Z., Bergen van, M.J., White, W.M., Varekamp, J.C., 1993. Sr-Nd-Pb isotope systematics of the Banda arc, Indonesia: combined subduction and assimilation of continental material. Journal of Geophysical Research 98, 22349–22366. https://doi.org/10.1029/93JB01716.
Walowski, K.J., Wallace, P.J., Hauri, E.H., Wada, I., Clynne, M.A., 2015. Slab melting beneath the Cascade Arc driven by dehydration of altered oceanic peridotite. Nature Geoscience 8, 404–408. https://doi.org/10.1038/ngeo2417.
Wang, Z.H., 2002. The origin of the cretaceous gabbros in the Fujian coastal region of SE China: Implications for deformation-accompanied magmatism. Contributions to Mineralogy and Petrology 144, 230–240. https://doi.org/10.1007/s00410-002-0392-3.
Wang, Z.H., Lu, H.F., 1999. Sm-Nd isochron age of the cumulate gabbro from the Fujian coastal region, Southeastern China, and its implication. Geological Review 45, 22–33 (in Chinese with English abstract).
Wang, F.Y., Ling, M.X., Ding, X., Hu, Y.H., Zhou, J. Bin, Yang, X.Y., Liang, H.Y., Fan, W.M., Sun, W., 2011. Mesozoic large magmatic events and mineralization in SE China: Oblique subduction of the Pacific plate. International Geology Review 53, 704–726. https://doi.org/10.1080/00206814.2010.503736.
Waters, L.E., Lange, R.A., 2015. An updated calibration of the plagioclase-liquid hygrometer-thermometer applicable to basalts through rhyolites. American Mineralogist 100, 2172–2184. https://doi.org/10.2138/am-2015-5232.
Watt, S.F.L., Pyle, D.M., Mather, T.A., Naranjo, J.A., 2013. Arc magma compositions controlled by linked thermal and chemical gradients above the subducting slab. Geophysical Research Letters 40, 2550–2556. https://doi.org/10.1002/grl.50513.
Weis, D., Kieffer, B., Maerschalk, C., Pretorius, W., Barling, J., 2005. High-precision Pb-Sr-Nd-Hf isotopic characterization of USGS BHVO-1 and BHVO-2 reference materials. Geochemistry, Geophysics, Geosystems 6. https://doi.org/10.1029/2004GC000852.
White, W.M., Dupré, B., 1986. Sediment subduction and magma genesis in the Lesser Antilles: Isotopic and trace element constraints. Journal of Geophysical Research 91, 5927. https://doi.org/10.1029/JB091iB06p05927.
Workman, R.K., Hart, S.R., 2005. Major and trace element composition of the depleted MORB mantle (DMM). Earth and Planetary Science Letters 231, 53–72. https://doi.org/10.1016/j.epsl.2004.12.005.
Xu, X.S., Dong, C.W., Li, W.X., Zhou, X.M., 1999. Late Mesozoic intrusive complexes in the coastal area of Fujian, SE China: the significance of the gabbro-diorite-granite association. Lithos 46, 299–315. https://doi.org/10.1016/S0024-4937(98)00087-5.
Zhang, G.W., Guo, A.L., Wang, Y.J., Li, S.Z., Dong, Y.P., Liu, S.F., He, D.F., Cheng, S.Y., Lu, R.K., Yao, A.P., 2013. Tectonics of South China continent and its implications. Science China Earth Sciences 56, 1804–1828. https://doi.org/10.1007/s11430-013-4679-1.
Zhang, L., Ren, Z.Y., Nichols, A.R.L., Zhang, Y.H., Zhang, Y., Qian, S.P., Liu, J.Q., 2014. Lead isotope analysis of melt inclusions by LA-MC-ICP-MS. Journal of Analytical Atomic Spectrometry 29, 1393–1405. https://doi.org/10.1039/c4ja00088a.
Zhang, L., Ren, Z.Y., Xia, X.P., Li, J., Zhang, Z.F., 2015. IsotopeMaker: a Matlab program for isotopic data reduction. International Journal of Mass Spectrometry 392, 118–124. https://doi.org/10.1016/j.ijms.2015.09.019.
Zhao, J.H., Hu, R.Z., Liu, S., 2004. Geochemistry and genesis of Daiqianshan gabbro, Fujian Province. Acta Mineralogica Sinica 24, 245–252 (in Chinese with English abstract).
Zhou, X.M., Li, W.X., 2000. Origin of late Mesozoic igneous rocks in Southeastern China: Implications for lithosphere subduction and underplating of mafic magmas. Tectonophysics 326, 269–287. https://doi.org/10.1016/S0040-1951(00)00120-7.
Zhou, X.M., Sun, T., Shen, W.Z., Shu, L.S., Niu, Y.L., 2006. Petrogenesis of Mesozoic granitoids and volcanic rocks in South China: a response to tectonic evolution. Episodes 29, 26–33. https://doi.org/10.18814/epigsi/2006/v29i1/62224.